Available online at www.sciencedirect.com

ScienceDirect

Underground Space 25 (2025) 33–53

www.keaipublishing.com/undsp

Integrated geophysical and computational modeling of hydromechanical mechanisms of underground debris flows in mining region

Yu Zhang [a], Kun He [a,b,*], Xiewen Hu [a,b], Wenlian Liu [c,d], Sugang Sui [c,d], Gang Luo [a,b], Mei Han [e]

[a] *Faculty of Geosciences and Engineering, Southwest Jiaotong University, Chengdu 611756, China*
[b] *Sichuan Province Engineering Technology Research Center of Ecological Mitigation of Geohazards in Tibet Plateau Transportation Corridors, Chengdu 611756, China*
[c] *Kunming Prospecting Design Institute of China Nonferrous Metals Industry Co., Ltd., Kunming 650032, China*
[d] *Key Laboratory of Geotechnical Engineering and Geological Disasters of Yunnan Province, Kunming 650032, China*
[e] *School of Mathematics, Southwest Jiaotong University, Chengdu 611756, China*

Received 31 March 2025; received in revised form 6 June 2025; accepted 9 June 2025
Available online 25 September 2025

Abstract

Underground debris flows, arising from the complex interplay of anthropogenic activities and rainfall-induced hydromechanical processes, present significant geotechnical hazards that remain poorly understood due to their hidden nature and dynamic multiphase triggers. Focusing on underground debris flow in a mining area in Southwest China, this study advances an integrated framework combining air-ground transient electromagnetic method (AGTEM) and computational fluid dynamics coupled with the discrete element method (CFD–DEM), revealing the migration mechanism in which microscale multiphase hydraulic erosion drives the macroscopic initiation of underground debris flow. Key findings include: (1) The identification of three transport phases (rapid erosion, slow erosion, and stabilization) provides actionable thresholds for monitoring and mitigation. (2) The coupled feedback between hydraulic conductivity anisotropy and the formation of preferential flow is the primary driver of large-scale debris transportation. (3) Linking mining-induced seismic energy to vibration-induced liquefaction via DEM simulations offers a physics-based explanation for flow mobilization triggers. The integrated geophysical-numerical framework offers new capabilities for predicting initiation thresholds and developing physics-based mitigation strategies in mining-affected terrains.

Keywords: Underground debris flow; Multiphase hydromechanical coupling; Hydraulic erosion; AGTEM; CFD–DEM

1 Introduction

Underground debris flows, a unique type of debris flow disaster caused by anthropogenic mining activities (Niu et al., 2023, 2024), have often been ignored due to their similarity in disaster effects to tunnel mud inrushes. Underground debris flow results in cascading destruction caused by coupling hydro-mechanical process. Rainwater infiltration destabilizes the surface deposits, while mining-induced structural damage to the ore layers forms fracture zones. Under hydraulic forces, surface sediments invade the underground mined-out areas through these fracture channels, endangering the safety of underground operations and substantially compromising the ecological environment. However, the disaster formation mechanisms of underground debris flows have not yet been fully studied, particularly the evolution characteristics of the migration

* Corresponding author at: Faculty of Geosciences and Engineering, Southwest Jiaotong University, Chengdu 611756, China.
E-mail address: hekun@swjtu.edu.cn (K. He).
Peer review under the responsibility of Tongji University

https://doi.org/10.1016/j.undsp.2025.06.002

pathways of underground debris flows, and the migration response mechanisms under mining vibrations and hydraulic conditions remain significant gaps in the research.

The initiation and transportation of underground debris flows are governed by multi-phase interactions between fluid pressure, fracture networks, and stress-driven rock mass degradation (Ren et al., 2021; Yin et al., 2021; Deng et al., 2023). Initiation typically emerges from localized fluidization of loose moraine or backfill materials, triggered by intense rainfall or groundwater influx that elevates pore pressures beyond thresholds (He et al., 2022, 2023; Zhang et al., 2024). During transportation, these mixtures mobilize along pre-existing or mining-induced fractures, where fracture roughness modulates the flow dynamics and ultimately dictates the flow regimes and internal blockages (Yin et al., 2021; Ren et al., 2024). However, during the formation and migration of underground debris flows, the feedback between fracture zone grids and particles remains difficult to quantify (Ren et al., 2025; Zhang et al., 2025). This is particularly true for the evolutionary characteristics of the coarse-grained skeletal structure of rock under fine particle erosion and the contact interactions between particles in the nonlinear flow process, which are hard to clearly explain. This significantly hinders the exploration of the dynamic mechanisms behind underground debris flow disasters. It emphasizes the necessity of combining geological-mechanical behavior of fracture grids at the macroscopic scale with multiphase particle flow models at the microscopic scale.

The migration of underground debris flow is a process in which surface fine particulate undergoes permeation and internal erosion within fracture zones (Zhang et al., 2020, 2021). Previous research has demonstrated that internal erosion within soil masses is a significant factor contributing to catastrophic events such as landslides and dam breaches (Crosta & Di Prisco, 1999; Danka & Zhang, 2015; Yang et al., 2020; Lei et al., 2017). Internal erosion predominantly manifests as the displacement of fine particles from the soil skeleton due to hydraulic activity, resulting in alterations to both the hydraulic characteristics and mechanical properties of the soil (Hu et al., 2019; Huang et al., 2021; Chen & Zhang, 2023). Previous research on internal erosion has focused primarily on laboratory experiments investigating the influence of soil particle size distribution on the internal stability of soil matrices, and criteria for assessing soil internal stability have been proposed on the basis of characteristic parameters (Kezdi, 1969; Kenney & Lau, 1986; Wan & Fell, 2008; Andrianatrehina et al., 2016). Furthermore, the effects of factors such as hydraulic gradient intensity, seepage flow direction, and stress state on the internal erosion of soil have been comprehensively examined (Deng et al., 2023; Sterpi, 2003; Marot et al., 2020; Liang et al., 2020). In recent years, X-ray computed tomography (CT) has also been applied to investigate the microstructural characteristics during internal erosion (Nguyen et al., 2019; Guo & Cui, 2020). However, the high cost of experimental procedures poses significant challenges to the widespread application of this method. To explore the interaction mechanisms between particles and fluids at the microscale, the coupled computational fluid dynamics-discrete element method (CFD–DEM) approach has been increasingly employed in simulation studies (Hu et al., 2021, 2023; Ma et al., 2021). Compared with the finite element method, the CFD–DEM offers enhanced capabilities for simulating particle movement and interactions within a seepage field, thereby providing a more accurate reconstruction of internal erosion phenomena. Oueidat et al. (2021) studied the effects of soil structural heterogeneity and fine particle percentage on the initiation of suffusion for multilayer gap-graded soil. Yin et al. (2021) established a 3D discrete element fluid flow sequentially coupled model to simulate fluid flow through a porous medium and calculate the transport of soil solids. Zhang et al. (2023) employed CFD–DEM to reveal the mechanisms of seepage erosion in fractured soil under cyclic hydraulic loads. Sun et al. (2023) analyzed the erosion mechanisms and evolution patterns of loess tunnels via CFD–DEM. Liu et al. (2021) focused on soil heterogeneity and flow field nonuniformity in the suffusion of gap-graded soils and provided micromechanical insights into this phenomenon.

Typically, the permeation and erosion of fine particles is a microscopic manifestation of the migration of underground debris flow. To fully reveal the migration mechanisms behind underground debris flow, it is crucial to also explore the macroscopic spatial distribution characteristics and evolution of the debris flow slurry. Due to its high concealment, underground debris flow cannot be detected through conventional geological methods (Yan et al., 2023, 2025). Relying solely on the unresolved CFD–DEM of fine particles is insufficient for explaining the macroscopic evolution of underground debris flow. Transient electromagnetic method (TEM), based on the electrical conductivity differences of geological bodies, offers a geophysical exploration technique that detects underground conductors to interpret complex geological formations (Qian, 2017; Xue et al., 2020). TEM has been widely used in the advanced prediction of tunnel water and mud inrushes (Li et al., 2018, 2024). Air-ground transient electromagnetic method (AGTEM), with its strong penetration capability and high sensitivity to fluid-saturated, low-resistivity structures, is particularly effective for detecting small-scale anomalies (karst features or fault zones) over large areas and complex terrains (Li et al., 2025). This provides an excellent tool for interpreting underground debris flow in fractured mining zones. However, previous research rarely integrates geophysical detection with numerical modeling to comprehensively address underground debris flows. A critical step toward overcoming these challenges is to establish a framework model for underground debris flow by integrating macroscopic geomechanical behaviors with microscopic multiphase par-

ticle flow, underpinned by the coupling feedback mechanism between fractured meshes and particle flow derived from numerical simulations.

This study focuses on an underground debris flow case in a mining area in Southwest China, and the migration mechanisms of underground debris flow are investigated through an innovative framework that integrates AGTEM resistivity profiling with a coupled CFD–DEM. The AGTEM provides field-scale mapping of conductive anomalies associated with fluid-saturated fracture zones, and the spatial evolution characteristics of the underground debris flow migration zone were revealed at a macroscopic scale. Complementing this, the CFD–DEM reveals the hydraulic erosion mechanisms during the migration of underground debris flow and dynamic response mechanisms under mining vibrations at a microscopic perspective, exploring the microscopic mechanisms driving the occurrence of macroscopic hazards. The findings provide critical insights for the design of geophysical monitoring systems and offer a scientific basis for the prevention and early warning of cascading failures in vulnerable mining areas.

2 Material and method

For the migration mechanisms of underground debris flows, this study first uses AGTEM to investigate the planar and vertical spatial distribution characteristics of the slurry migration area within the study area, thereby revealing the spatiotemporal evolution mechanisms of underground debris flows at a macroscopic scale (Fig. 1(a)). Additionally, CFD–DEM is utilized to reveal the permeation and erosion mechanisms of fine moraine particles under hydraulic action at a microscopic scale, exploring the microscopic mechanisms driving the occurrence of macroscopic hazards (Fig. 1(b)). Subsequently, a comprehensive analysis of the migration characteristics and evolution patterns of underground debris flow is carried out.

2.1 Case study

2.1.1 Study area

The study area is located in a large metal mining region in northwestern Yunnan, China (Fig. 2). The exposed strata in the mining area primarily consist of Quaternary moraine deposits (Q_4^{gl}), with the main rock type being quartz diorite porphyrite, alongside gray slate from the Tumugou Formation (T_3^t). The mining area has a high elevation landform, with the elevation ascending from west to east and ranging from 3840 to 4633 m above sea level. The terrain on both sides exhibits pronounced steepness, resulting in a V-shaped valley characterized by significant river downcutting, which is characteristic of deeply incised

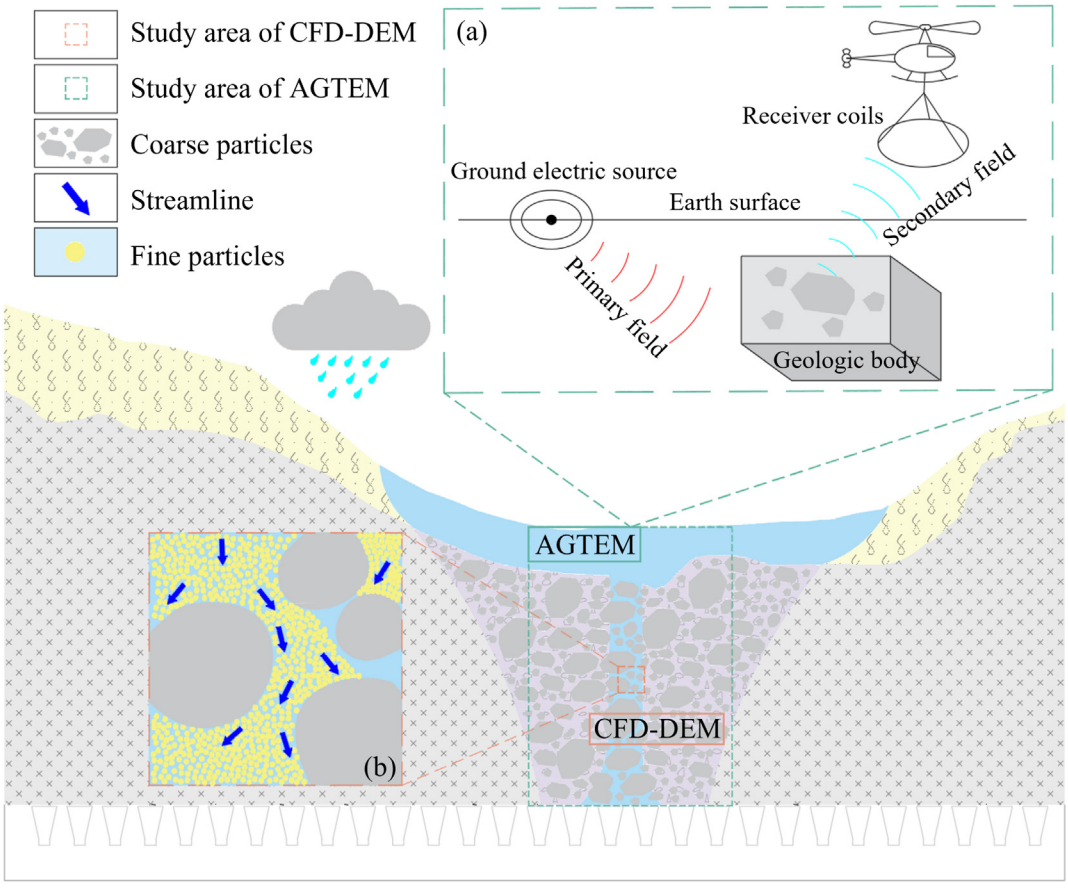

Fig. 1. Schematic diagram of the integrated ACTEM and CFD–DEM framework.

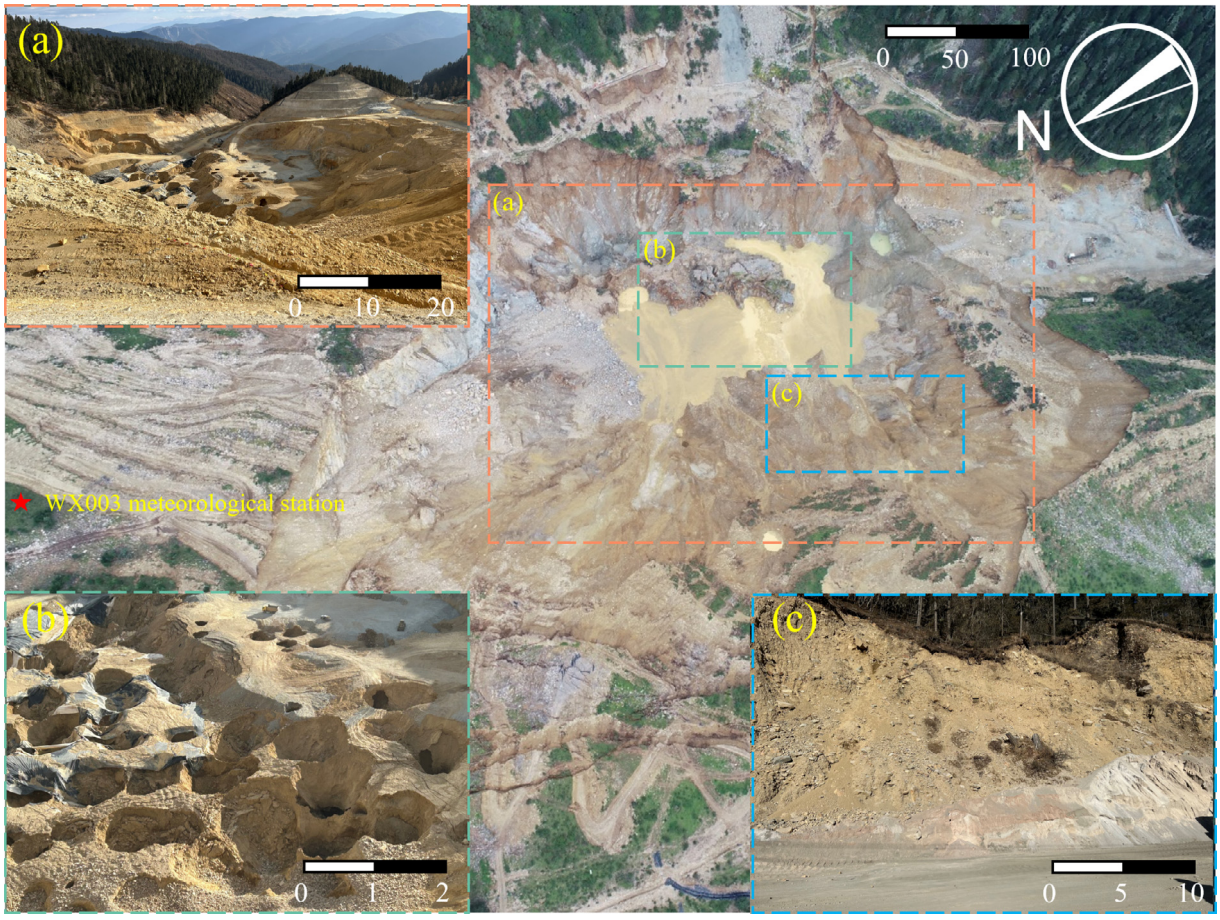

Fig. 2. Orthoimages of the study area (September 2019). (a) Subsidence area (January 2022), (b) mining-induced surface sinkholes, and (c) surface Quaternary moraine soil layer. (Unit: m)

alpine landforms. Since the mining area is near a surface watershed, the terrain is heavily dissected, with well-developed faults, secondary folds, and joint fractures. Atmospheric precipitation is the sole source of groundwater recharge. The region experiences an average annual rainfall of 619.9 mm, primarily concentrated between June and September, accounting for 87.1% of the total annual precipitation.

2.1.2 Characteristics of underground debris flows

As a result of rainfall and surface confluence, loose surface deposits are mobilized and accumulate in areas of subsidence caused by surface mining. They migrate into underground spaces through pores and fracture channels generated by mining activities, ultimately leading to the formation of underground debris flows (Fig. 3). Due to mining activities and concentrated rainfall, the study area has experienced multiple underground debris flow events since 2019 (Fig. 4). The maximum deposit volume reached 9500 m^3 for a single event, severely impacting production equipment and compromising the safety of operational personnel.

Field investigations of underground debris flows in the study area indicate that, similar to conventional debris flows, three essential conditions must be met with respect to topographical conditions, water source availability, and material source accessibility. The extensive subsidence areas provide favorable topographical conditions for the accumulation of rainfall and moraine soils (Fig. 5(a)). Continuous and concentrated rainfall provides the necessary water source for the formation of slurry (Fig. 5(c)), while the loose Quaternary moraine distributed on the surface provides the material source conditions for the formation of underground debris flows (Fig. 5(b)).

However, different from tunnel water and mud inrush, the solid material source of underground debris flows is primarily composed of loose moraine distributed on the surface, consisting mostly of fine-grained particles with better sorting but poor erosion resistance. When these fine particles migrate through fracture zones composed of broken ore, two types of particles exhibit distinctly different movement characteristics. The involvement of water further accentuates these differences in movement. Regrettably, the current understanding of the migration mechanisms of underground debris flows is based solely on reasonable inferences from field investigation, and it fails to explain the mechanical behavior characteristics and spatiotemporal evolution mechanisms during the

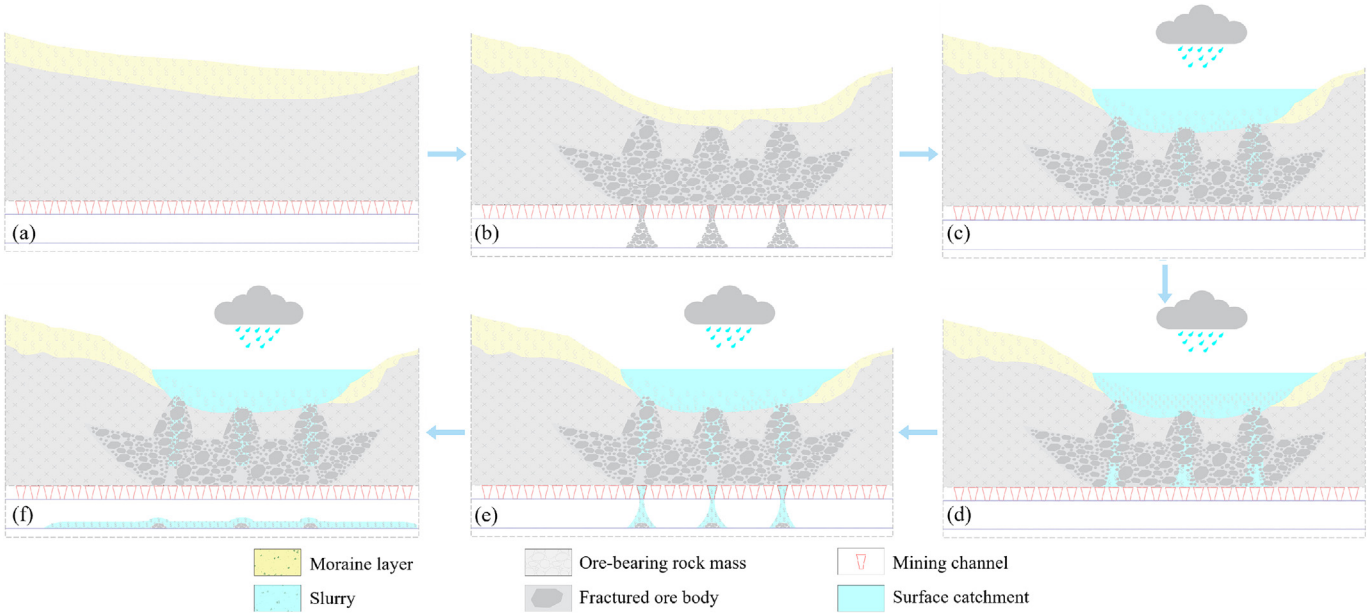

Fig. 3. Formation process of underground debris flows. (a) Initial state, (b) surface subsidence caused by mining, (c) after the rainfall, slurry forms inside the subsidence crater and downward seepage erosion along the mineral seam, (d) slurry migrates into the goaf interior through seepage erosion, (e) mining operations trigger the outbreak of underground debris flow, and (f) underground debris flows spread and deposit along the mining tunnel.

Fig. 4. Underground debris flow burying the tunnel. (a) August 2019, (b) November 2019, (c) underground debris flow destroying mining facilities, and (d) underground debris flow leading to ore dilution.

migration process of underground debris flows. Therefore, revealing the formation mechanisms of underground debris flows should be explored from two perspectives: the spatiotemporal evolution mechanisms of debris flow migration at the macroscopic scale and the permeation and erosion behavior of particles at the microscopic scale.

2.2 Method

2.2.1 Air-ground transient electromagnetic method

The AGTEM was used to investigate the planar and vertical distribution of slurry in the study area. The geophysical survey employed the ZT-30 high-power DC trans-

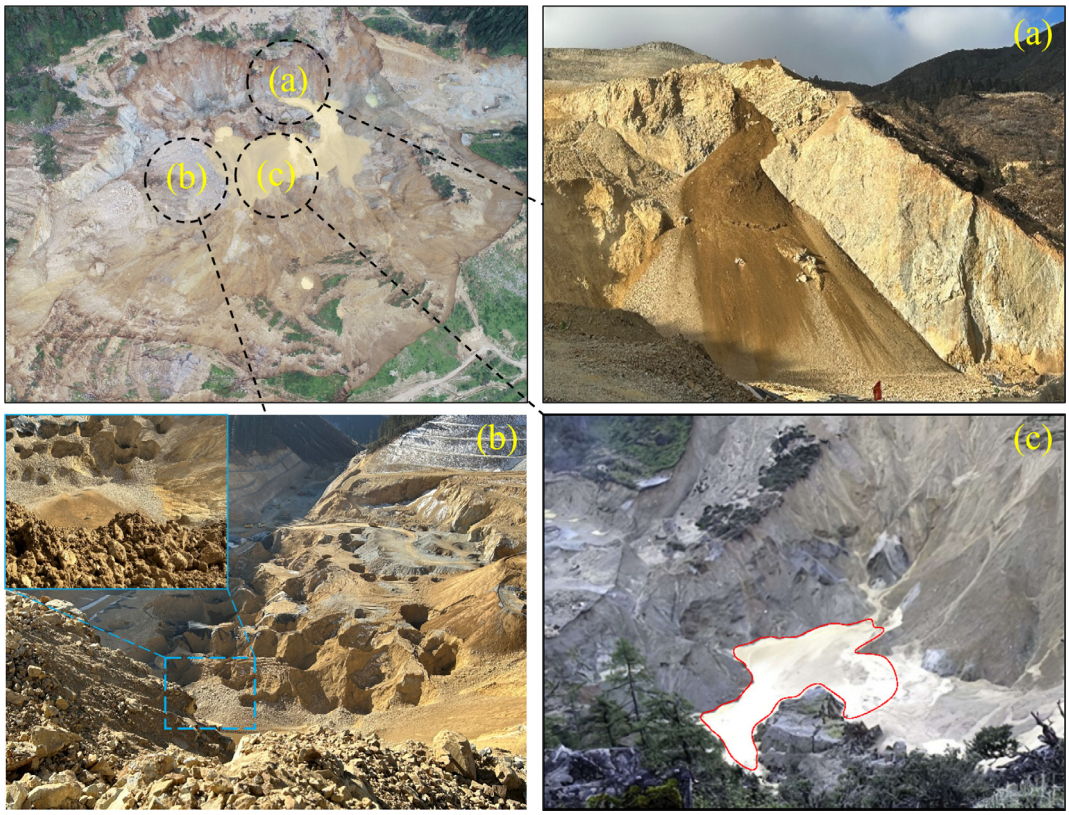

Fig. 5. Conditions for underground debris flow. (a) Steep slopes surrounding the subsidence areas, (b) the rainwater mixes with loose moraine soils within the subsidence area to form a slurry, and (c) loose moraine soils move down the slope toward the subsidence area.

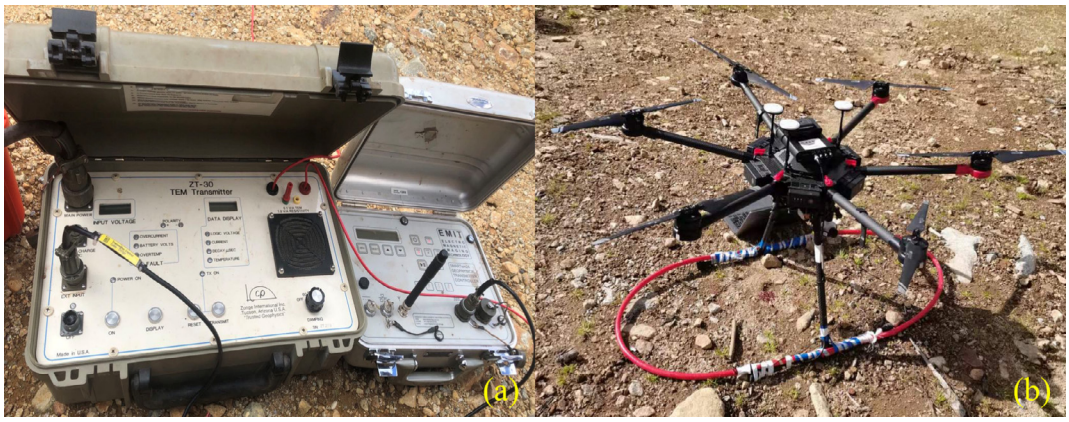

Fig. 6. AGTEM instrument. (a) ZT-30 high-power DC transmitter and SM24 transmitter controller, and (b) DJI M600 Pro multirotor UAV.

mitter from Zonge International (Fig. 6(a)) and the SM24 transmitter controller from Australia ElectroMagnetic Imaging Technology (Fig. 6(b)). A DJI M600 Pro multirotor unmanned aerial vehicle (UAV), equipped with an X3 camera and gimbal, was used for flight-based data acquisition. The survey grid had a spacing of 20 m × 10 m, with a total of 615 measurement points analyzed (Fig. 7). The overall root mean square relative error for the entire survey was 9.42%.

2.2.2 Coupled CFD–DEM method

In practical engineering, the rate of internal erosion is exceedingly slow, making it impractical to utilize CFD–DEM simulations for long-term assessments of internal erosion. To optimally replicate the evolution process of internal erosion while also considering computational capabilities, during the construction of the model, it is essential to consider the effects of model size and particle quantity to ensure that the model satisfies the fundamental

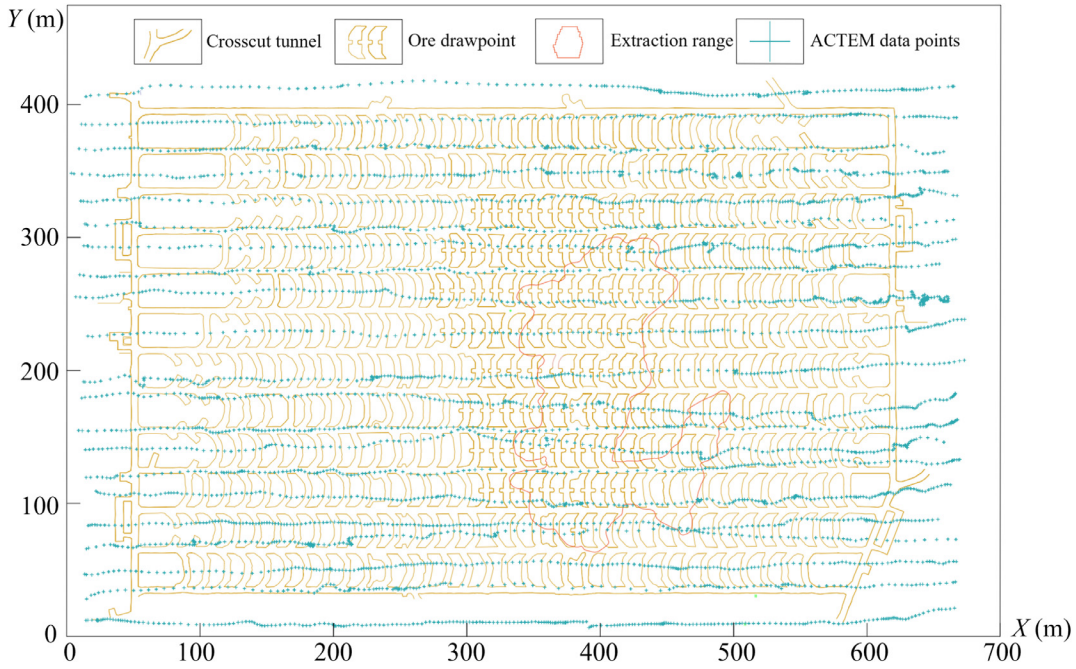

Fig. 7. Distribution of AGTEM measurement points (elevation 3720 m).

conditions for internal erosion. Furthermore, an appropriate hydraulic gradient must be selected to facilitate the rapid development and stabilization of internal erosion, thereby achieving the objective of resource conservation.

In the analysis of internal erosion, the fluid phase is analyzed by solving the Navier–Stokes equations based on a multiphase flow model, which captures the flow characteristics of the continuous medium in a multiphase environment (Moukalled et al., 2016). Meanwhile, particle motion is governed by the linear contact model in the DEM, which simulates interparticle interactions such as collision and friction. The mass and momentum equations are:

$$\frac{\partial n_1}{\partial t} + (\nabla n_1 \bar{v}) = 0, \tag{1}$$

$$\frac{\partial (n_1 \bar{v})}{\partial t} + \nabla n_1 \bar{v}\ \bar{v} + \frac{n_1}{\rho}(\nabla p + \nabla c) - n_1 - \frac{f_{\text{int}}}{\rho} = 0, \tag{2}$$

where n_1 is the local porosity; $\bar{v}$ is the average fluid velocity; ∇p is the fluid pressure gradient; ρ is the fluid density; c represents the internal friction force; and f_{int} is the fluid drag force.

In the CFD–DEM coupled model, the fluid phase is solved on a fixed Eulerian mesh, while individual particles are tracked using the DEM within a Lagrangian framework to determine their positions, velocities, and force states. At each time step, the DEM provides particle-scale kinematic information, which is used to compute the local porosity and particle volume fraction within each CFD cell. These values are then applied to locally average the interaction forces between the fluid and particles (drag, buoyancy, and pressure gradient forces). The resulting porosity-corrected body forces are subsequently transferred to the CFD module, where the fluid velocity field and fluid-particle interaction forces are computed by solving the Navier–Stokes equations and pressure gradient equations. The fluid forces calculated in the CFD module are then fed back to the DEM as body forces acting on the particles, driving their motion in the next step. Through this iterative procedure, two-way momentum exchange and coupling between the fluid and particles are achieved (Hu et al., 2019; Kawano et al., 2018; Ma et al., 2021; Xiong et al., 2021). In this study, the open-source CFD code OpenFOAM (https://www.openfoam.org) is employed for simulating the fluid phase, while the PFC3D program is used to simulate the solid particle behavior, and the coupling between CFD and DEM is implemented in the PFC3D program (Itasca Consulting Group, 2018). To maintain computational efficiency and numerical stability, the CFD timestep is set as 100 times the DEM timestep (Yin et al., 2021). Figure 8 depicts the flow chart of the employed CFD–DEM method.

2.2.2.1 Model setup.

Internal erosion is caused primarily by the movement of soil particles under hydraulic conditions, leading to the loss of fine particles along the soil pores with flow. The migration of fine particles alters the size and content of pores within the soil body, thereby affecting the internal seepage field of the soil. The internal erosion behavior is driven by complex fluid particle interactions that are influenced by multiple factors, such as soil gradation, pore distribution, hydraulic conditions, and stress state. However, establishing and analyzing an internal erosion model that is completely consistent with physical experiments would

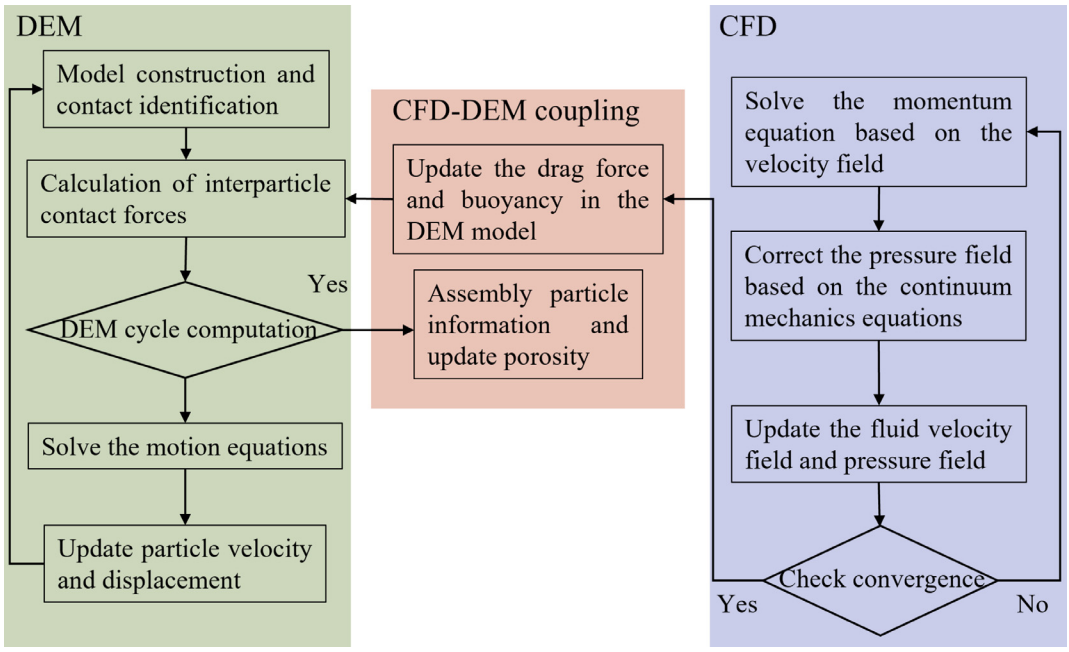

Fig. 8. Flow chart of the adopted CFD DEM method.

require the generation of millions of particles, which far exceeds the computational capabilities of current computers. Therefore, to more accurately represent the microstructural characteristics of fine particles during their migration, necessary simplifications should be implemented when constructing the model.

Internal erosion requires a disparity in particle size, where the pores between coarser particles provide channels for the migration of fine particles. By incorporating the gradation curve of moraine soils from the study area, simulations were conducted using the particle sizes shown in Fig. 9. The diameters of fine particles ranged from 0.10 to 0.25 mm, and the diameters of coarse particles ranged from 1 to 2 mm, resulting in a gap ratio of 8. On the basis of the definitions of coarse and fine soil components established by Kezdi (1969), this soil is classified as gap-graded moraine soil, that is, internally unstable soil. Three types of gap-graded glacial till were selected for the simulation. The main difference among these three moraine soils lies in the content of fine particles, with fine particles accounting for mass fractions of 15%, 25%, and 35%.

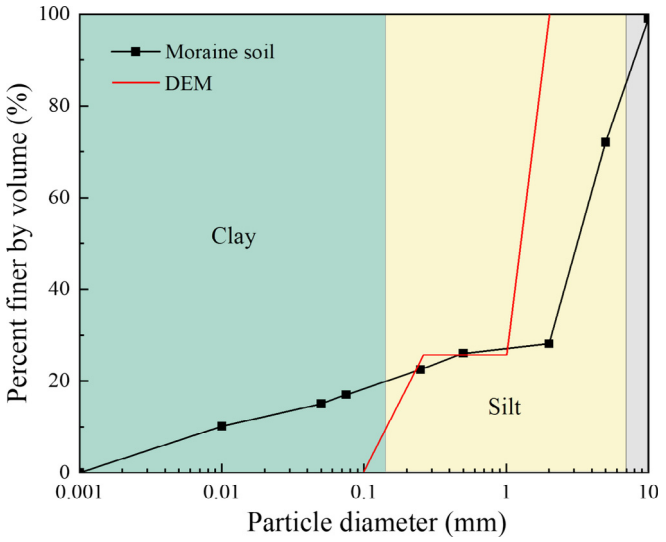

Fig. 9. Particle size distribution.

To ensure the accuracy of the computational results while conserving computational resources as much as possible, this paper uses a rectangular model composed of spherical particles and measuring 6 mm × 6 mm × 12 mm. The ratio of the model dimensions to the largest particle diameter is greater than 5, effectively eliminating the influence of boundary effects. The model comprises a total of 38 610 particles, including 214 coarse particles and 38 396 fine particles (Fig. 10(a)). To ensure the uniformity of the fluid, the CFD region completely covers the DEM boundary and has dimensions of 6 mm × 6 mm × 16 mm (Fig. 10(b)). During the internal erosion process, the bottom wall of the model is replaced with a filter mesh to restrict the passage of coarse particles. The ratio of the filter pore size to the fine particle size is 5, ensuring that fine particles can pass through smoothly.

2.2.2.2 Determination of model parameters.

Reasonable parameters are an essential foundation for ensuring the accuracy of simulations. Model parameters were calibrated through triaxial compression test simulations conducted under the same confining pressures as laboratory tests (Fig. 11(a)). A linear contact model was adopted to simulate interparticle interactions within the moraine, and axial loading was applied by controlling the

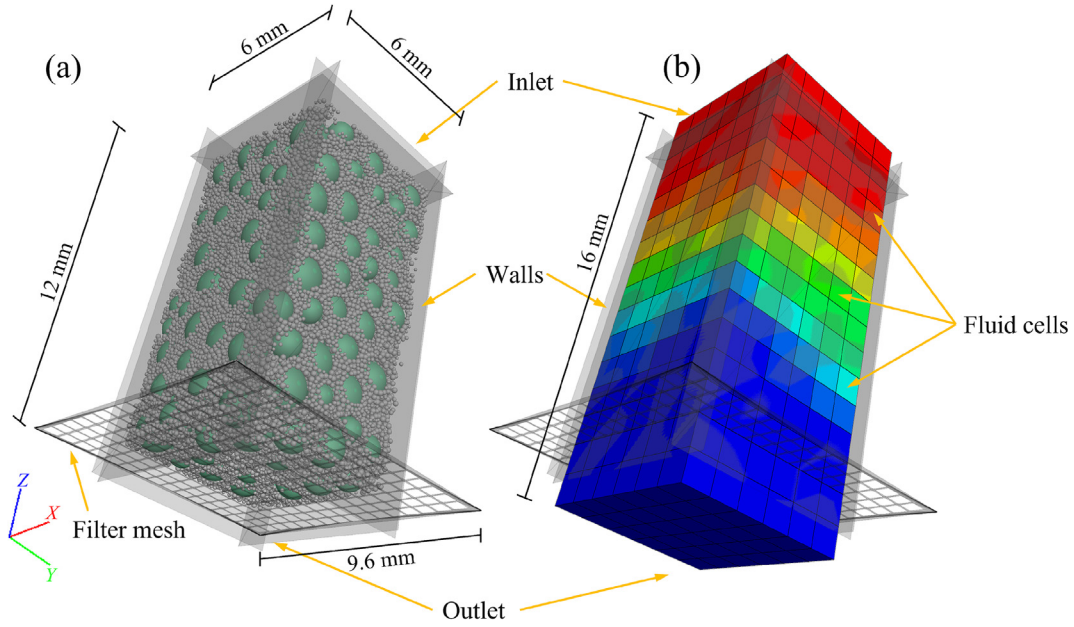

Fig. 10. Setup of the DEM and CFD computations. (a) Particle model, and (b) fluid model.

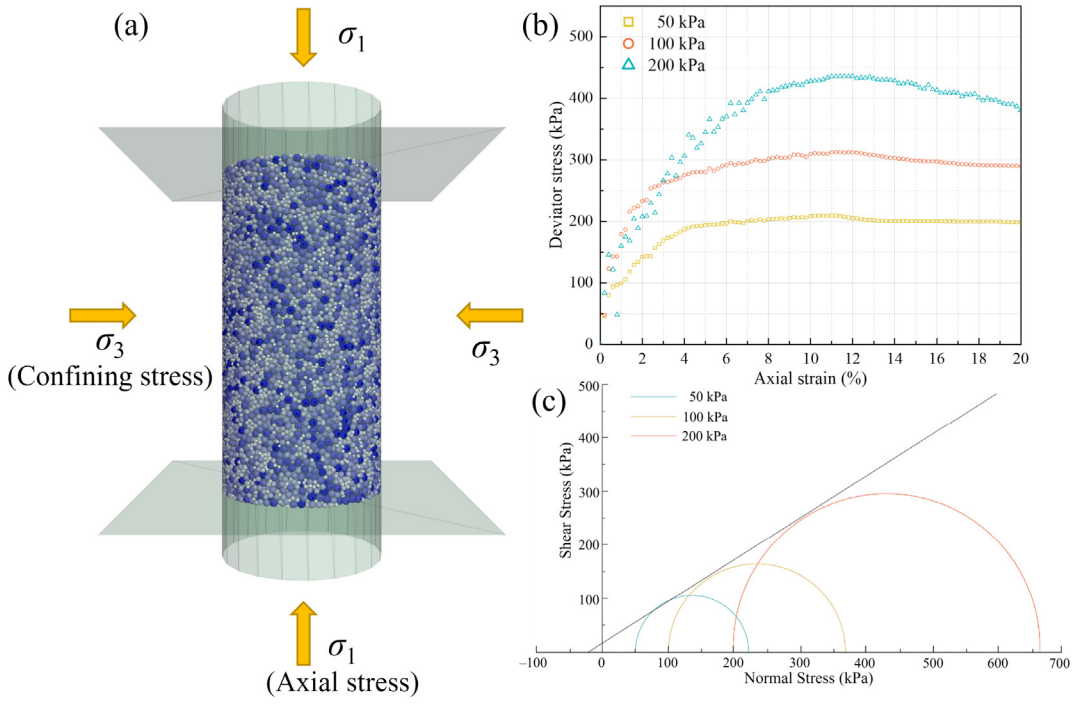

Fig. 11. Calibration of simulation parameters. (a) Numerical triaxial test model, (b) stress–strain curves, and (c) Mohr's circle.

movement of the upper and lower loading plates. Prior to the simulation, empirical parameters (stiffness ratio, friction coefficient) were selected based on relevant literature (Chang et al., 2021; Sun et al., 2023). The bond strength parameters were then adjusted to match the peak stress, and the stress–strain curve was obtained (Fig. 11(b)). The macroscopic mechanical strength parameters were compared with laboratory tests. When the error exceeded 10%, the parameters were recalculated until they met the prescribed accuracy range. Based on the simulation results under three confining pressures, the Mohr's circle under triaxial compression was prepared (Fig. 11(c)). The determined shear strength parameters are shown in Table 1. The microscopic parameters used in the simulation are presented in Table 2. Since the explicit integration method in the DEM module is employed in this study, to ensure the converged solution of coupled pressure–velocity fluid phase equations, the DEM time step is set as 2.0×10^{-7} s, while

Table 1
Comparison of the simulated and measured microscopic parameters of the models.

Type	Measured value		Simulated value	
	Cohesion (kPa)	Internal friction angle (°)	Cohesion (kPa)	Internal friction angle (°)
Values	12.23–21.40	34.86–39.82	17.2	37.8

Table 2
Input microscopic parameters used in the seepage erosion simulation.

Computation modules	Parameter types	Values
Solid system (DEM)	Particle density (kg/m^3)	2190
	Elastic modulus (kPa)	1.0×10^5
	Bond stiffness ratio	1.2
	Friction coefficient (particle–particle)	0.5
	Friction coefficient (particle–wall)	0.0
	Damping coefficient	0.1
	Coefficient of friction	0.5
Fluid system (CFD)	Fluid density (kg/m^3)	1.0×10^3
	Fluid viscosity (Pa•s)	1.0×10^{-3}
Fluid-particle interaction (CFD–DEM)	Timestep of DEM (s)	2.0×10^{-7}
	Timestep of CFD (s)	2.0×10^{-5}
	Simulation real time (s)	6.0×10^4

the fluid computation time step is set as 2.0×10^{-5} s (Norouzi et al., 2016; Mehdizadeh et al., 2021; Mu et al., 2023). Some of the parameters related to particles and fluids are taken from previous studies (Zhao et al., 2014; Tang et al., 2017; Zou et al., 2020; Peng et al., 2014).

2.2.2.3 Boundary conditions.

To simulate unidirectional flow conditions, initial fluid pressure is applied at both ends of the CFD model. The top boundary of the CFD model is set as the inflow boundary, and the bottom boundary is set as the outflow boundary. Moreover, considering a larger critical hydraulic gradient for narrower soil grading, a larger absolute hydraulic gradient is adopted ($i = 2$) to ensure the occurrence of erosion (Mu et al., 2023). The lateral boundaries are set as free slip boundaries with transverse displacement constraints. Due to the uneven spatial distribution of particles, the variability in the permeability distribution of the models leads to fluctuations in the hydraulic head distribution (Fig. 9(b)). Numerical simulations were carried out using a computer with an I9-13900 K CPU and 128 GB of RAM. The total computation time for the model was 54 h.

3 Results

3.1 Air-ground electrical distribution characteristic

Figures 12 and 13 show the planar and profile apparent resistivity distribution map of the study area at different elevations. It can be observed that the apparent resistivity ranges between 100 and 1000 Ω·m, with the red and orange areas representing high resistivity zones. The resistivity distribution is uniform, which is interpreted as the electrical response of the intact ore body. In contrast, the apparent resistivity ranges from 0.01 to 60.00 Ω·m, with the green and dark blue areas indicating apparent resistivity anomalies. This suggests that in these areas, the rock mass is not only more fractured but also filled with slurry, leading to extremely low apparent resistivity. This is interpreted as the electrical response of slurry-filled fractured rock zones. Additionally, the area of the apparent resistivity anomaly increases with elevation, indicating that the slurry filling range becomes larger as it approaches the surface. This suggests that the underground debris flow migration primarily occurs through the rock mass fracture zones, moving downward from the surface subsidence area, while the fractured rock mass caused by natural caving mining provides a good transport channel for the migration.

The apparent resistivity profile map more clearly illustrates the distribution characteristics of underground debris flow migration pathways. Influenced by mining activities in the crosscut tunnel at the 3720 m level (Fig. 13), the upper rock mass structure becomes increasingly fractured, gradually evolving into a continuous fracture zone connecting the surface and subsurface. Concurrently, a large-scale surface subsidence area is formed. Under continuous and concentrated rainfall, rainwater accumulates with loose moraine within the surface subsidence area, forming slurry, which is characterized by extremely low apparent resistivity in the subsidence area. The slurry then gradually migrates along the fractured zone

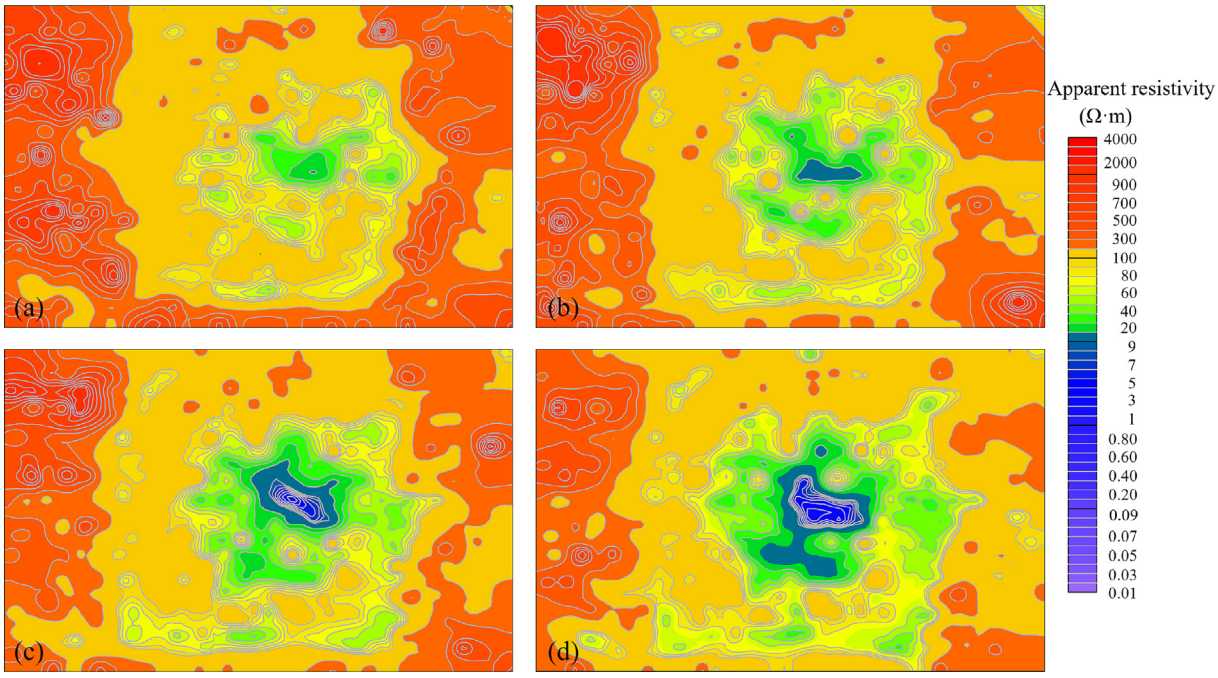

Fig. 12. Apparent resistivity planar distribution. (a) Elevation 3730 m, (b) elevation 3750 m, (c) elevation 3770 m, and (d) elevation 3790 m.

into the mined-out area, continuously filling the fractured zone, resulting in a large anomalous apparent resistivity zone in the ore-bearing rock mass beneath the subsidence area. As the slurry accumulates extensively within the ore bin, subsequent mining disturbances trigger its sudden rush into the crosscut tunnel along with collapsed ore, forming an underground debris flow.

3.2 Erosion characteristics

Under hydraulic action, fine moraine particles move downward through the pores at a velocity higher than that of coarse mineral particles, reaching the maximum velocity at $t = 2$ s (Fig. 14(a)). This phenomenon can be attributed to the size disparity between mineral particles and moraine particles, wherein the pores among mineral particles serve as channels for the movement of fine moraine particles. At $t = 4$ s, due to the blockage of fine particles in the pore channels, the velocity of some moraine particles begins to decrease. At $t = 10$ s, some fine particles have completed the internal erosion process and flow out through the filter mesh, whereas others reach a state of equilibrium after blocking the channels, resulting in their velocity being reduced to zero.

Particle mass loss during internal erosion is one of the key indicators for assessing the erosion effect (Lei et al., 2017; Yang et al., 2020). To quantify the internal erosion pattern of fine moraine particles over time, the particle mass erosion rate, ζ, is used to reflect changes in the particle erosion state. ζ is calculated as shown in Eq. (3). In the simulation, fine particles that migrate through the bottom filter mesh are considered to be eroded particles.

$$\xi = \frac{m_{\text{eroded}}}{m_{\text{total}}}, \tag{3}$$

where m_{eroded} is the mass of eroded particles; m_{total} is the mass of total particles.

Four measuring spheres with a diameter of 6 mm were vertically delineated within the model to obtain the curve of porosity changes over time within the spheres (Fig. 15). Overall, the internal erosion process can be divided into three stages: (1) rapid erosion phase, (2) slow erosion phase, and (3) stabilization phase. During the rapid erosion phase, fine moraine particles commence movement in the direction of flow under hydraulic action, driven by seepage forces. Fine particles located near the bottom are rapidly eroded, resulting in the interconnection of pores within the skeleton of coarse mineral particles. The velocity of fine particle migration increases rapidly, forming stable preferential flow paths along the pore channels. In this state, both the particle mass erosion rate and porosity of the soil exhibit a rapid increasing trend. During the slow erosion phase, the average flow velocity of fine particles begins to decrease as they are gradually eroded and transported out of the soil mass. Meanwhile, the pore volume within the soil increases, and the seepage channels remain largely stable. Fine particles in localized areas reach a state of equilibrium due to blockage, resulting in a slowdown in the rate of increase in both the particle mass erosion rate and porosity. In the stabilization phase, a large number of fine particles have already been eroded, and the seepage force exerted by the fluid is insufficient to continue moving the remaining particles blocked in the pores. At this point, the soil reaches a stable state, with no further changes in the mass erosion rate or porosity. This is highly consistent

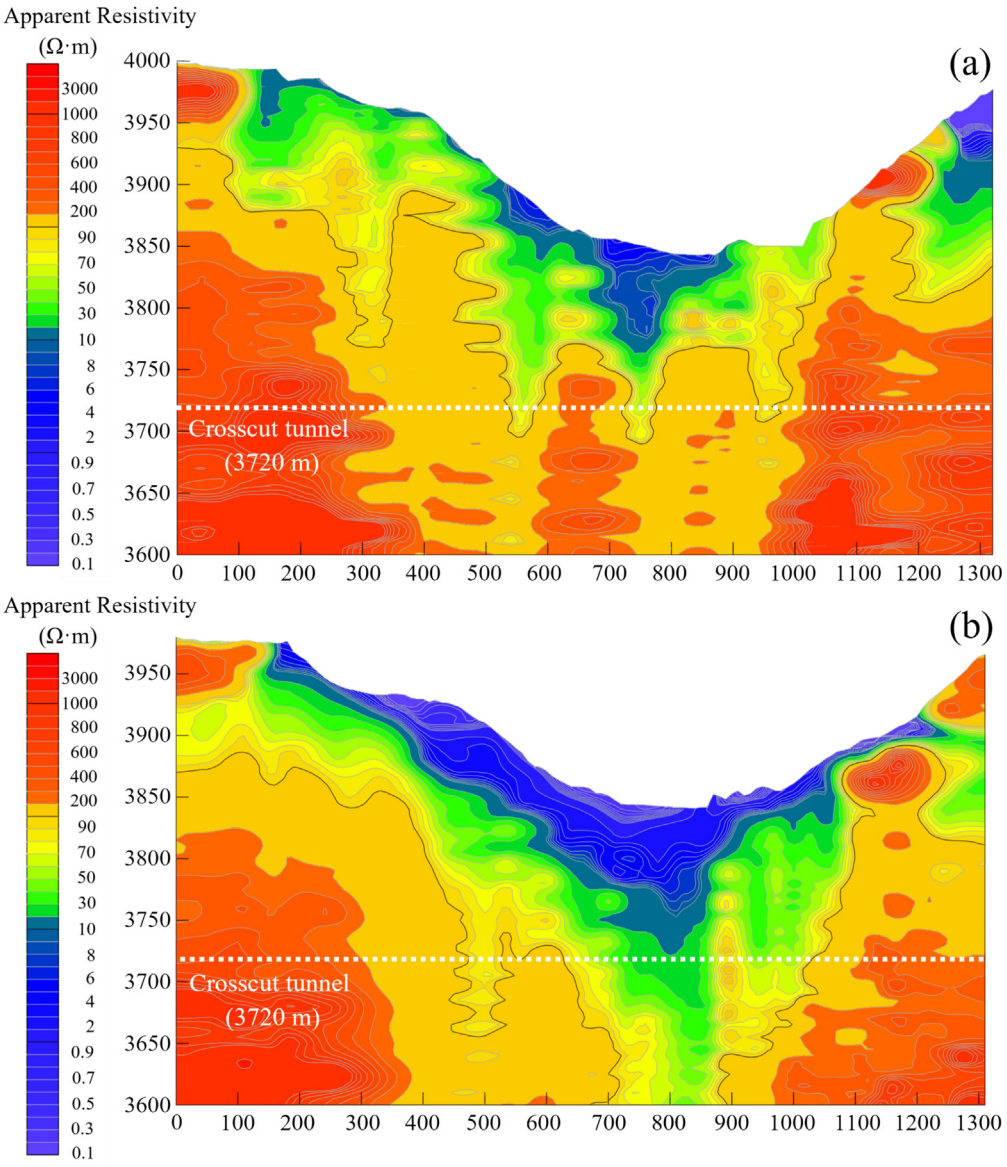

Fig. 13. Apparent resistivity profile distribution. (a) North-south profile, and (b) south-east profile.

with the studies reported by Yin et al. (2021) and Sun et al. (2023). On the one hand, the gap graded samples composed of moraine particles and ore bodies are particularly susceptible to erosion under hydraulic loading that exceeds the critical gradient. In the rapid erosion phase, the erosion rate exhibits a nonlinear increase, followed by a sharp decline and stabilization as fine particles are lost and local clogging occurs. On the other hand, compared with the results conducted by Yin et al. (2021) and Sun et al. (2023), under similar hydraulic conditions, the final erosion rate and local porosity observed in this study are significantly lower. This discrepancy is mainly attributed to the smaller particle size ratio and higher fine particle content in the present model, which hinders the erosion process. Additionally, the greater axial length of the model results in longer migration paths for fine particles in this study, further contributing to the observed differences.

The internal erosion process encompasses several technical aspects, including particle detachment, particle migration, alterations in the soil skeleton structure, and localized pore blockage. Alterations in localized features are crucial to the evolution of internal erosion effects. Fine moraine particles exhibit different movement characteristics in local areas during internal erosion, influenced by the mineral skeleton. Slices of the model at various heights were analyzed to obtain the distribution characteristics of fine particles in the upper (h_3), middle (h_2), and lower (h_1) layers of the model during different erosion stages (Fig. 16). During the period of 0–5 s, erosion occurs in the soil without significant changes to the mineral skeleton. Some coarse mineral particles form dominant seepage channels, resulting in the rapid loss of fine moraine particles, which intensifies erosion in that area. This stage is the primary phase of the erosion process. Simultaneously,

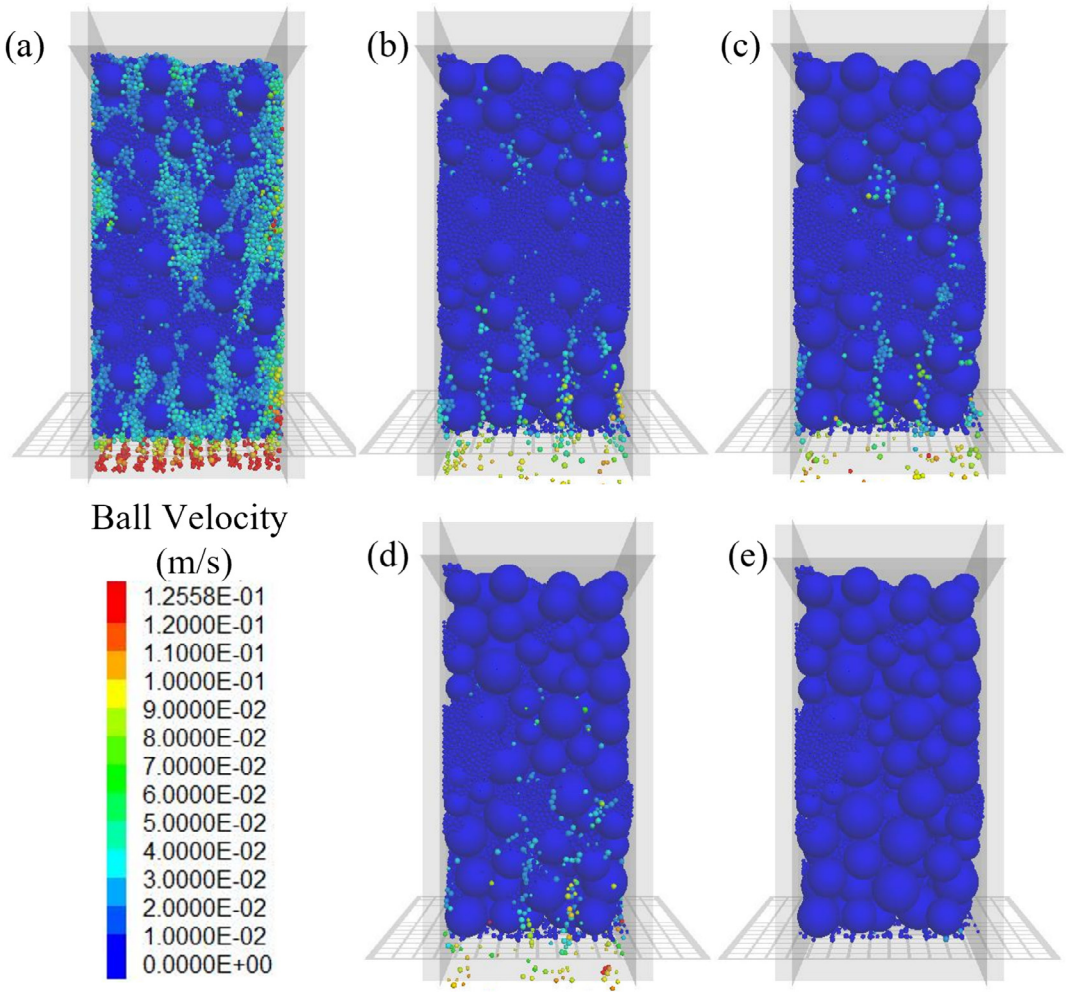

Fig. 14. Velocity of the particles. (a) $t = 2$ s, (b) $t = 4$ s, (c) $t = 6$ s, (d) $t = 8$ s, and (e) $t = 10$ s.

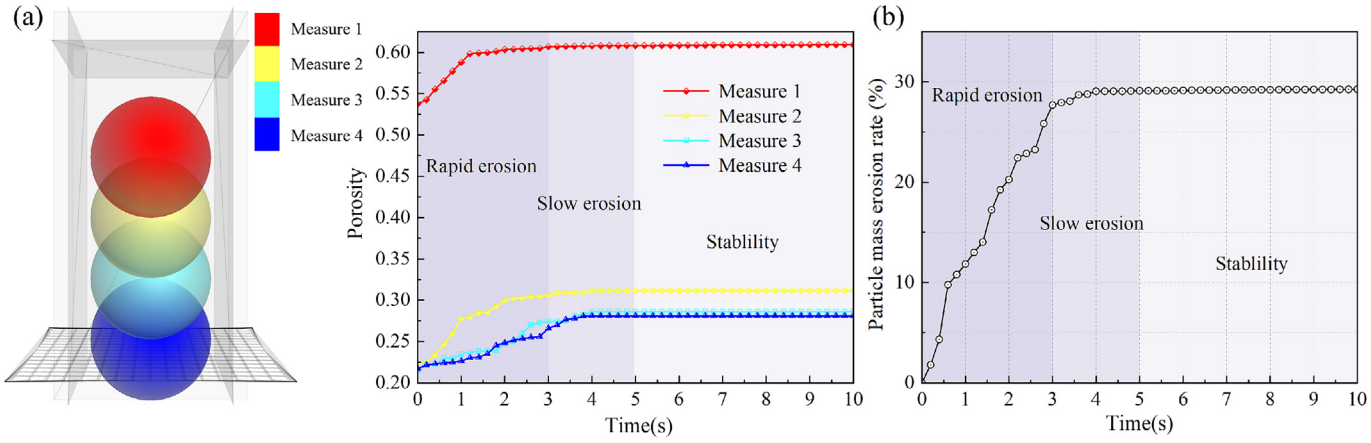

Fig. 15. Changes in particle mass erosion rate and porosity. (a) Porosity, and (b) particle mass erosion rate.

some pore channels become blocked due to the concentrated accumulation of fine particles, thereby preventing further movement of fine particles and, to a certain extent, slowing erosion. After $t = 5$ s, the internal erosion process is in the stabilization phase, and the structure of the pore channels within the mineral essentially remains stable, with only sporadic fine moraine particles seeping out under the influence of the flow field. According to the slice analysis

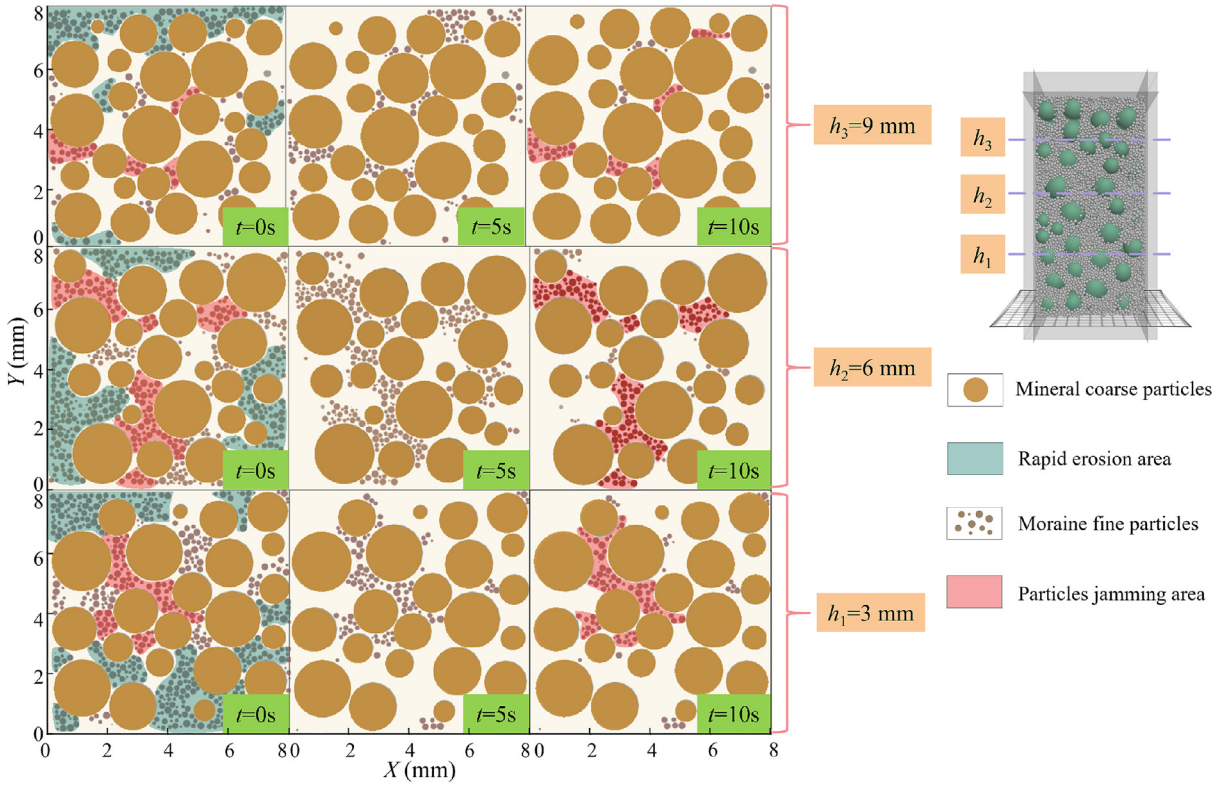

Fig. 16. Slice analysis of the particle distribution at different times.

(Fig. 16), the loss of fine particles is greatest in the upper part of the soil, which is most significantly affected by erosion. In contrast, the degree of erosion in the middle part of the soil is relatively minor due to the longer migration paths of fine particles and the noticeable blockage effect of particles in the pores of some coarse particle skeletons.

Figure 17 shows the evolution of local porosity in the vertical direction before and after erosion. In the initial stage of erosion, local porosity is evenly distributed along the longitudinal axis, ranging between 0.21 and 0.23. However, after erosion, as fine particles are lost, the porosity in the model exhibits a significant increasing trend. The most pronounced increase in local porosity occurs near the lower boundary of the model (0–6 mm), where the maximum local porosity reaches 0.6. The second largest increase is observed at the upper boundary (11–12 mm), while the middle-upper region of the model (7–10 mm) experiences the smallest increase, with a maximum local porosity of 0.3. This indicates that under erosion, the accumulation and clogging effects of the pore channels are concentrated in the middle-upper region of the model, whereas the dominant seepage channels primarily develop near the lower boundary.

As fine particles migrate during erosion, the distribution characteristics of the seepage field also change. Figure 18 illustrates the flow velocity distribution at different erosion stages. Before erosion occurs, the velocity vectors are relatively uniform in direction, and the flow velocity remains stable (Fig. 18(a)). During the subsequent stage of intense

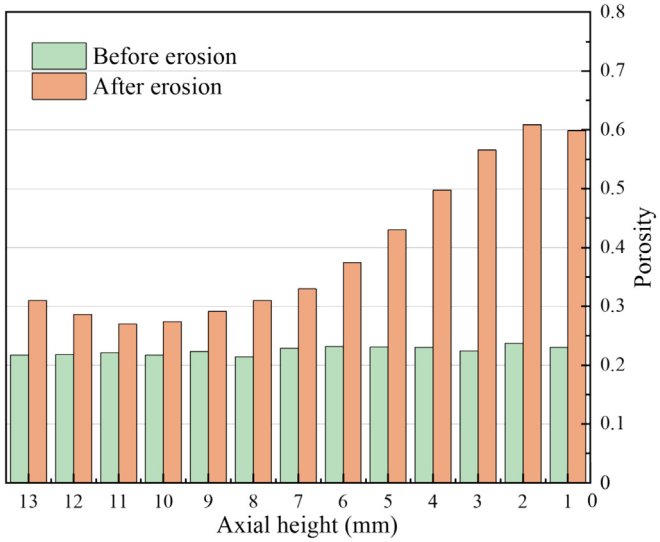

Fig. 17. Variation of the local porosity of the model along the vertical direction.

erosion, significant changes occur in both the direction and magnitude of the local flow field. As fine particles are rapidly eroded, the porosity between coarse particles increases, resulting in variations in hydraulic conductivity within the soil skeleton. This leads to the formation of localized preferential seepage channels in regions where fine particle loss occurs, causing a significant increase in fluid velocity in those areas (Fig. 18(c)). Meanwhile, some

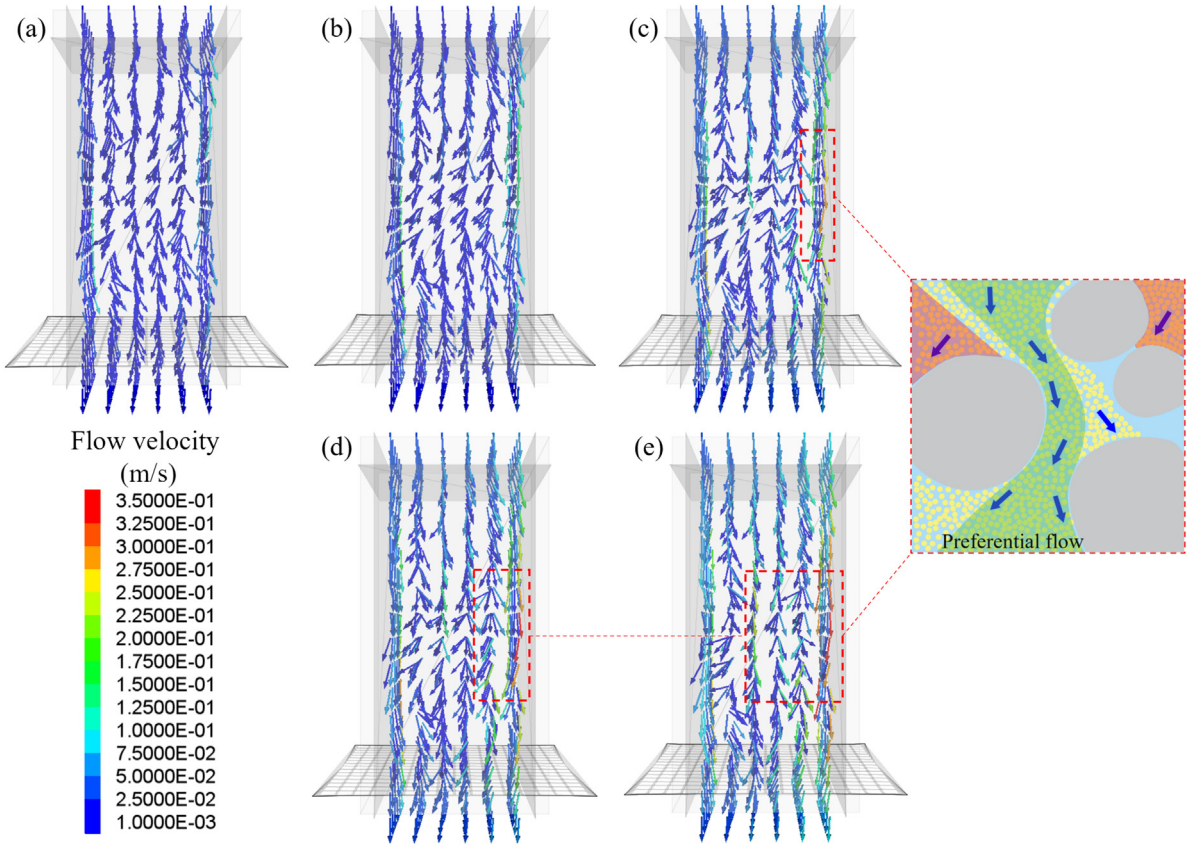

Fig. 18. Evolution of the fluid velocity. (a) $t = 2$ s, (b) $t = 4$ s, (c) $t = 6$ s, (d) $t = 8$ s, and (e) $t = 10$ s.

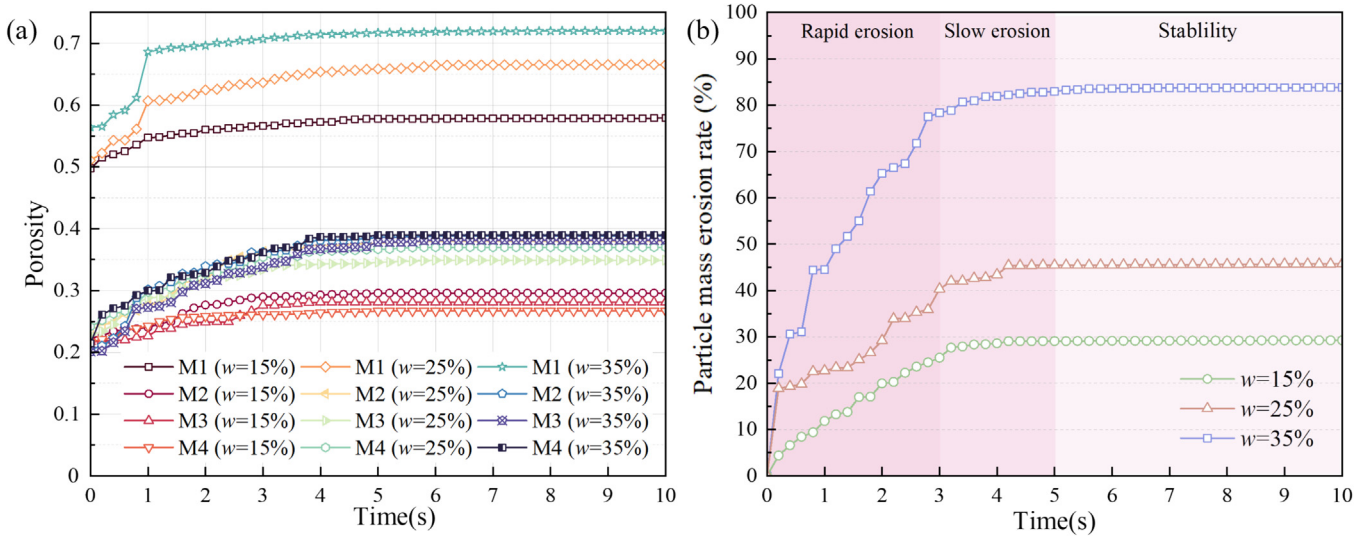

Fig. 19. Changes in particle erosion rate and porosity with different fine particle mass fractions. (a) Porosity, and (b) particle mass erosion rate.

pore channels become blocked due to the accumulation of fine particles, causing a shift in the flow direction while maintaining a stable velocity. Under the combined effect of these two processes, the phenomenon of hydraulic conductivity anisotropy is further intensified. During the slow erosion phase and stability phase, fine particles reach an equilibrium state in some areas due to clogging, while stable preferential seepage channels form in others. At this stage, the flow field gradually stabilizes under the influence of erosion, and the velocity vectors exhibit a non-uniform distribution in both direction and magnitude (Fig. 18(e)). It is evident that hydraulic conductivity anisotropy serves

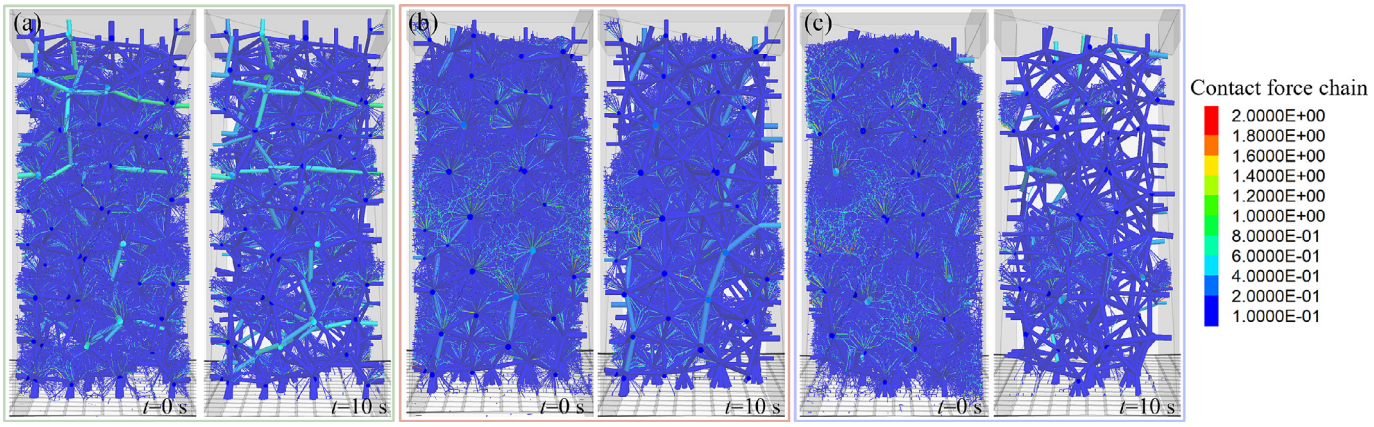

Fig. 20. Contact force chains with different fine particle mass fractions. (a) $w = 15\%$, (b) $w = 25\%$, and (c) $w = 35\%$.

as both a prerequisite and a driving factor for the formation of preferential flow, while the development of preferential flow further intensifies local hydraulic conductivity anisotropy and internal erosion. This positive feedback between the two processes facilitates the progression of internal erosion.

3.3 Influence of the fine particle content

The internal stability of soil varies due to its structural properties, heterogeneity, and discontinuity. Previous studies have shown that the dominant factor affecting the stability of soil during the internal erosion process is the proportion of fine particles within the soil (Zhang et al., 2023; Sun et al., 2023). The response mechanisms of internal erosion vary among soils with different fine particle contents, due to differences in the composition of the soil skeleton and permeability. Analysis of the variation patterns of internal erosion indicators within the measuring spheres (M1–M4 represent four measuring spheres) under three different fine particle mass fractions reveals that as the content of fine particles increases, both the internal porosity and the final particle erosion rate show a significant increasing trend (Fig. 19). In soil with a high content of fine particles, the final particle mass erosion rate reaches 83.83%, resulting in complete destruction of the soil. This occurs because when the content of fine particles exceeds a certain threshold (the optimum content of fine particles), it becomes difficult for the soil to form a stable skeleton structure. The pore channels between coarse particles cannot be tightly filled by fine particles, which, to a certain extent, increases the permeability inside the soil. However, when the content of fine particles is reduced, the pore channels inside the soil are more densely filled, significantly enhancing the internal stability of the soil under hydraulic action.

The internal contact force between particles is key to controlling the internal erosion process. By using simulation software, the micro-mechanisms of internal erosion in soil can be analyzed with respect to the types of internal particle contacts and the resulting contact force chains.

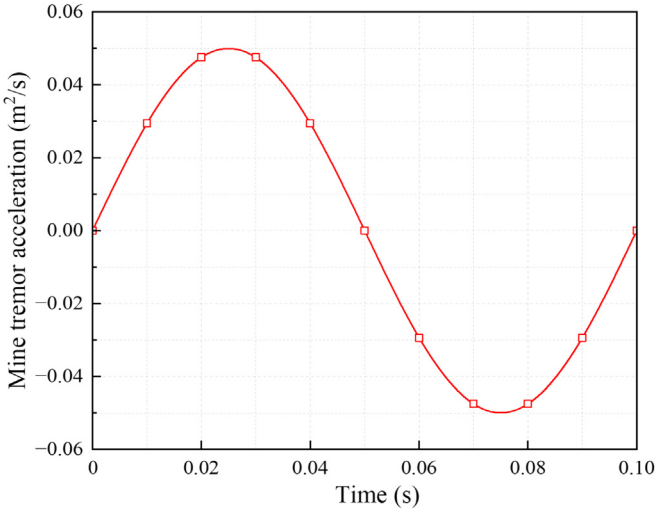

Fig. 21. Input horizontal wave acceleration-time curves.

Changes in the mass fraction of fine particles, w, primarily affect the structural characteristics of the coarse mineral particle skeleton. From a microstructural perspective, different contents of fine particles determine the filling relationship between coarse and fine particles, thereby resulting in different internal erosion characteristics under various hydraulic gradients. When the content of fine particles is low, the pore channels are tightly filled by fine particles, and the contact force chains are primarily composed of coarse-coarse particle contacts. The fine particles lost after internal erosion mostly participate in the formation of weak contacts, whereas the strong contacts between coarse particles remain largely unchanged. Additionally, due to the restricting effect of the coarse particle skeleton, the amount of eroded fine particles is limited. Most fine particles are blocked within the pore channels, forming a new skeleton structure together with coarse particles (Fig. 20(a)). When the content of fine particles is moderate, fine particles essentially fill the pores between coarse particles, and the proportion of fine-fine particle contact force chains increases. Under the action of fluid, fine particle blockage occurs in the middle part of the soil, whereas fine

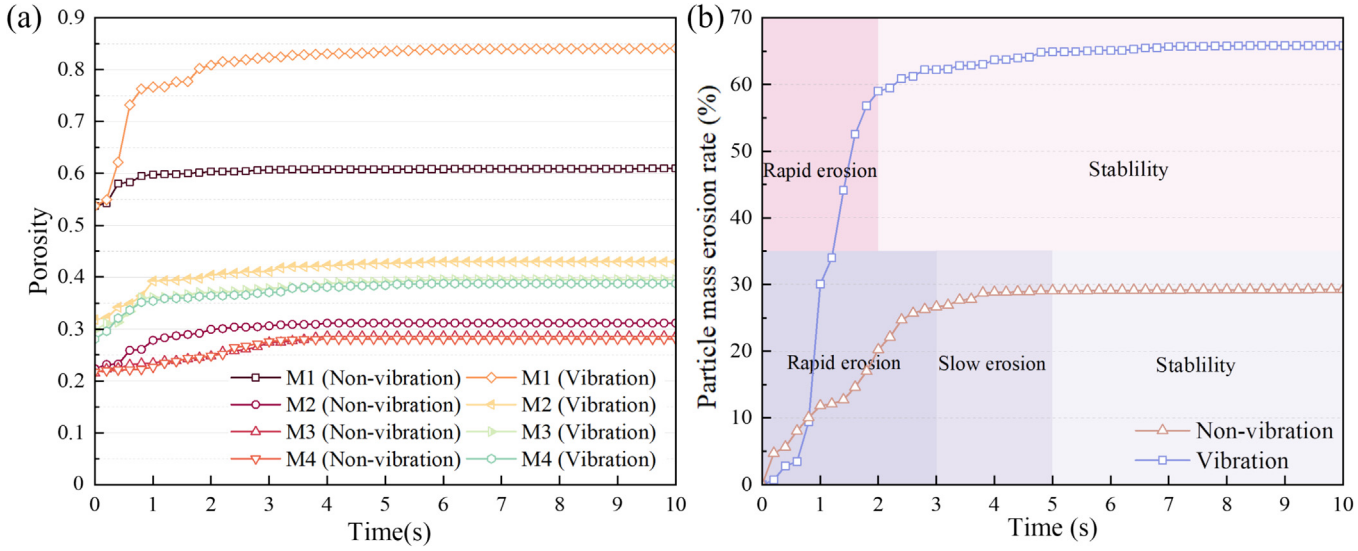

Fig. 22. Changes in particle mass erosion rate and porosity under vibration. (a) Porosity, and (b) particle mass erosion rate.

particles at the top and bottom are more strongly eroded (Fig. 20(b)). When the content of fine particles is high, the contact force chains are mainly composed of weak forces between fine-fine particles. The pores between coarse particles are essentially interconnected, with only a few pore channels being completely filled by fine particles. Most of the pore channels are not fully filled with fine particles and are unevenly distributed. Under the action of fluid, fine particles are more likely to detach from the coarse particle skeleton and migrate. Interconnected pores easily form preferential flow paths, significantly intensifying the erosion effect (Fig. 20(c)).

4 Discussion

4.1 Dynamic response of mining vibrations

The thick layer of moraine soil distributed on the surface provides a supply for underground debris flows through the action of internal erosion. Nevertheless, given the influence of factors such as the hydraulic gradient and moraine soil content, internal erosion as the sole source of materials for underground debris flows cannot fully explain the phenomenon of large-scale underground debris flows erupting multiple times in a short period in real engineering applications. The occurrence of underground debris flows is closely related to underground mining activities. In the study area, where the natural caving method is employed (Castro et al., 2007; Pierce, 2010), underground blasting and ore collapse not only alter the stress field distribution of the overlying strata but also impact the migration process of moraine soil. Therefore, it is necessary to analyze the dynamic response mechanism of internal erosion during the migration of moraine material sources to vibrations from underground mining activities.

The thickness of the ore in the study area reaches hundreds of meters, and the vibration waves generated by mining activities at the bottom of the mine attenuate quickly after passing through the ore. Therefore, the vibration waves used in the simulation have a small amplitude and low frequency (Yang et al., 2018; Tofany et al., 2019). The seismic vibration wave is simplified to a sinusoidal tensile acceleration wave with an amplitude of 0.05g and a frequency of 10 Hz (Fig. 21). The wave velocity of loose moraine generally ranges from 600 to 800 m/s. The vibration wavelength is 60–80 m, which is significantly larger than the model size. Therefore, the vibration wave parameters meet the propagation requirements within the model (Dou et al., 2021). Using a model with $w = 15\%$ for analysis, after generating particles and reaching servo equilibrium, the vibration wave is applied in the horizontal direction on the walls surrounding the model, with the walls set as viscous boundaries. The damping coefficient of the spherical particles is adjusted to 0.1 to fit the practical situation. By solving for the migration characteristics of fine moraine particles within 10 s, the dynamic response mechanism of the internal erosion effect of moraine material sources for underground debris flows under mining disturbance conditions is revealed (see Fig. 22).

The internal erosion effect is significantly intensified under vibration, with a distinct increasing trend in porosity and the final particle mass erosion rate compared to conditions without vibration. Furthermore, the internal erosion mechanism exhibits different characteristics under the influence of vibration waves. At $t = 1$–2 s, the internal erosion process is in the rapid erosion phase, and vibration causes an increase in the initial erosion rate. A large number of fine moraine particles are eroded during this stage. The pore channels formed between coarse mineral particles are not easily to be blocked by fine particles and remain stable under the influence of vibration waves, further intensifying the internal erosion effect. At $t = 2$–10 s, the soil is in the stabilization phase, and the fine moraine particles have essentially been eroded. It is evident that vibration

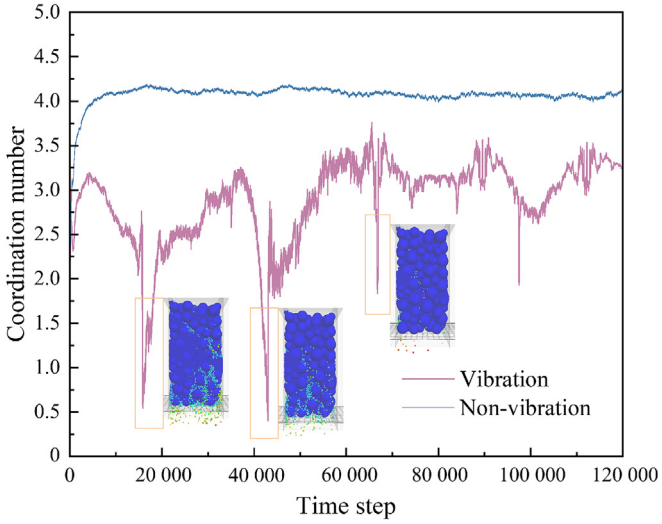

Fig. 23. Changes in average coordination number.

significantly impacts the internal erosion process, greatly weakening the blocking effect of fine moraine particles in the pore channels. This results in the internal erosion process exhibiting only the rapid erosion phase and the stabilization phase.

Indeed, the internal erosion process induced by vibration closely resembles the phenomenon of soil liquefaction. To characterize the microevolutionary features of particles during the fine particle erosion process, the changes in the distribution function of the average coordination number γ (the ratio of the total number of particles to the number of particle contacts) are analyzed to quantitatively describe the vibration response mechanism of fine moraine particles. Figure 23 illustrates the change in the average coordination number with increasing computational timesteps. Vibration reduces the average coordination number during internal erosion of the soil, indicating that vibration decreases the number of contacts between particles. Under conditions without vibration, the average coordination number shows a fluctuating increasing trend followed by stabilization. This is due to the movement of fine moraine particles between pore channels under hydraulic action. As fine particles are lost, the average coordination number of the model tends to stabilize. However, under conditions with vibration, the vibration causes a periodic steep decline in the average coordination number. Moreover, the fine moraine particles are in a liquefied state, and the fine particles and fluid in the pore channels form preferential flows, intensifying the internal erosion effect. As fine particles are removed, the contact forces between particles progressively diminish, leading to gradual stabilization of the coordination number.

4.2 Guidelines for mining operations, monitoring, and early warning

Based on the integrated geophysical-numerical framework employed in this study, it is evident that the rapid erosion stage plays a critical role in the initiation and evolution of underground debris flows. This stage is characterized by the rapid infiltration and migration of surface slurry through subsurface fissure networks, which leads to a sudden rise in local pore water pressure and anomalously high surface deformation rates. The short-term surface dynamic response during this phase can be captured by the 3D laser scanning monitoring stations deployed at the study site, which can serve as a surface deformation rate threshold for the rapid erosion stage in the monitoring and early warning system for underground debris flows. Meanwhile, the coupled feedback between preferential flow and hydraulic conductivity anisotropy is a primary driver of large-scale underground debris flow migration. The widespread uneven surface subsidence further confirms the presence of hydraulic conductivity anisotropy during the migration process. Therefore, in areas of severe surface deformation, necessary backfilling and grouting measures should be implemented to block hydraulic connectivity between the surface and subsurface. In addition, the current mining scheme should be adjusted to reduce the ore extraction volume in the corresponding underground mining areas, in order to mitigate surface differential subsidence. These integrated measures can greatly enhance the monitoring and control of underground debris flow in complex mining environments, while also informing regulatory guidelines for mining operations in vulnerable regions.

4.3 Limitations and future work

While the integrated AGTEM and CFD–DEM framework provides valuable insights into the migration mechanisms of underground debris flow, it still has certain limitations. First, while AGTEM is advantageous in identifying saturated fluids and fracture zones, its resistivity inversion results are constrained by electromagnetic interference and complex terrain, making it insufficient for accurately characterizing material composition and fluid properties. Comprehensive interpretation still requires the integration of drilling and other direct investigation methods. Second, to balance computational efficiency and model accuracy, the unresolved CFD–DEM method adopts simplified spherical particle assumptions and idealized boundary conditions. Additionally, seismic disturbances are modeled using idealized sinusoidal acceleration waves, which differ from the complex waveforms generated by actual mining blasts, thus limiting the accuracy of dynamic response analysis for underground debris flow migration. Future work should focus on integrating real-time data from mine-site 3D laser scanning monitoring stations into the proposed framework. By combining dynamic factors (surface deformation, vibration), an early-warning system that incorporates underground debris flow initiation thresholds can be developed.

5 Conclusions

By integrating AGTEM geophysical surveying with CFD–DEM modeling, this study effectively bridges macroscopic spatial characterization and microscopic particulate dynamics, offering a holistic framework for underground debris flow analysis. The main conclusions are as follows:

(1) Due to the continuous mining activities of the natural caving method, the through-going fracture zone forms between the surface and the crosscut tunnel. Rainwater and loose moraine accumulate in the surface subsidence area, forming a slurry that migrates downward along the fracture zone, resulting in a resistivity anomaly zone with an "inverted trapezoidal" distribution.
(2) According to the characteristic variations in the porosity and particle mass erosion rate, the internal erosion process can be divided into three main phases: rapid erosion phase, slow erosion phase, and stabilization phase. The coupled feedback between hydraulic conductivity anisotropy and the formation of preferential flow during the rapid erosion stage is the primary factor driving the large-scale migration of underground debris flow.
(3) The fine particle mass contents significantly influence the internal erosion process. As the fine particle mass content increases, the filling relationship between coarse and fine particles changes, and the type of particle contact shifts from primarily strong contacts between coarse particles to primarily weak contacts between fine particles, making the soil more susceptible to erosion and damage.
(4) Vibrations from underground mining activities significantly reduce the contact between particles, causing fine particles to exhibit a liquefied state. This facilitates the formation of preferential flows between pore channels, intensifying internal erosion. Moreover, vibration waves greatly weaken the blocking effect between pore channels, resulting in the internal erosion process comprising only the rapid erosion stage and the stabilization stage.

Data availability

The data that support the findings of this study are available from the corresponding author upon reasonable request.

CRediT authorship contribution statement

Yu Zhang: Software, Data curation, Methodology, Conceptualization, Writing – original draft, Investigation. **Kun He:** Validation, Methodology, Writing – review & editing. **Xiewen Hu:** Funding acquisition, Writing – review & editing, Conceptualization, Supervision. **Wenlian Liu:** Writing – review & editing. **Sugang Sui:** Writing – review & editing. **Gang Luo:** Writing – review & editing. **Mei Han:** Writing – review & editing.

Declaration of competing interest

The authors declare that they have no known competing financial interests or personal relationships that could have appeared to influence the work reported in this paper.

Acknowledgement

The authors gratefully acknowledge support from the National Natural Science Foundation of China (Grant Nos. 42377170 and 42407212), the Postdoctoral Fellowship Program of China Postdoctoral Science Foundation (Grant No. GZB20230606), the Postdoctoral Research Foundation of China (Grant No. 2024M752679), and the Sichuan Natural Science Foundation (Grant No. 2025ZNSFSC1205).

References

Andrianatrehina, L., Souli, H., Rech, J., Taibi, S., Fry, J. J., Ding, L., & Fleureau, J. M. (2016). Analysis of the internal stability of coarse granular materials according to various criteria. *European Journal of Environmental and Civil Engineering, 20*(8), 936–953.

Castro, R., Trueman, R., & Halim, A. (2007). A study of isolated draw zones in block caving mines by means of a large 3D physical model. *International Journal of Rock Mechanics and Mining Sciences, 44*(6), 860–870.

Chang, W. B., Wang, P., Wang, H. J., Chai, S. F., Yu, Y. F., & Xu, S. Y. (2021). Simulation of the Q2 loess slope with seepage fissure failure and seismic response via discrete element method. *Bulletin of Engineering Geology and the Environment, 80*, 3495–3511.

Chen, C., & Zhang, L. M. (2023). Hydro-mechanical behaviour of soil experiencing seepage erosion under cyclic hydraulic gradient. *Géotechnique, 73*(2), 115–127.

Crosta, G., & Di Prisco, C. (1999). On slope instability induced by seepage erosion. *Canadian Geotechnical Journal, 36*(6), 1056–1073.

Danka, J., & Zhang, L. M. (2015). Dike failure mechanisms and breaching parameters. *Journal of Geotechnical and Geoenvironmental Engineering, 141*(9), 04015039.

Deng, Z. Z., Wang, G., Jin, W., Tang, N., Ren, H. X., & Chen, X. S. (2023). Characteristics and quantification of fine particle loss in internally unstable sandy gravels induced by seepage flow. *Engineering Geology, 321*, 107150.

Dou, L. M., Cao, J. R., Cao, A. Y., Chai, Y. J., Bai, J. Z., & Kan, J. L. (2021). Research on types of coal mine tremor and propagation law of shock waves. *Coal Science and Technology, 49*(6), 23–31 (in Chinese).

Guo, C. X., & Cui, Y. F. (2020). Pore structure characteristics of debris flow source material in the Wenchuan earthquake area. *Engineering Geology, 267*, 105499.

He, K., Liu, B., Hu, X. W., Zhou, R. C., Xi, C. J., Ma, G. T., Han, M., Li, Y., & Luo, G. (2022). Rapid characterization of landslide-debris flow chains of geologic hazards using multi-method investigation: Case study of the Tiejiangwan LDC. *Rock Mechanics and Rock Engineering, 55*(8), 5183–5208.

He, K., Xi, C. J., Liu, B., Hu, X. W., Luo, G., Ma, G. T., & Zhou, R. C. (2023). MPM-based mechanism and runout analysis of a compound reactivated landslide. *Computers and Geotechnics, 159*, 105455.

Hu, J. Y., Ma, T., & Ma, K. (2021). DEM-CFD simulation on clogging and degradation of air voids in double-layer porous asphalt pavement under rainfall. *Journal of Hydrology, 595*, 126028.

Hu, Z., Zhang, Y. D., & Yang, Z. X. (2019). Suffusion-induced deformation and microstructural change of granular soils: A coupled CFD–DEM study. *Acta Geotechnica, 14*, 795–814.

Hu, Z., Li, J. Z., Zhang, Y. D., Yang, Z. X., & Liu, J. K. (2023). A CFD–DEM study on the suffusion and shear behaviors of gap-graded soils under stress anisotropy. *Acta Geotechnica, 18*, 3091–3110.

Huang, Z., Bai, Y. C., & Xu, H. J. (2021). A vertical layered theoretical model to predict the suffusion-induced heterogeneity of cohesionless soil. *Journal of Hydrology, 598*, 126476.

Itasca Consulting Group, Inc. (2018). Particle flow code in 3 dimensions. Ver. 5.0 User manuals. Itasca, Minneapolis, USA.

Kawano, K., Shire, T., & O'Sullivan, C. (2018). Coupled particle-fluid simulations of the initiation of suffusion. *Soils and Foundations, 58*(4), 972–985.

Kenney, T. C., & Lau, D. (1986). Internal stability of granular filters: Reply. *Canadian Geotechnical Journal, 23*(3), 420–423.

Kezdi, A. (1969). Increase of protective capacity of flood control dikes. *Department of Geotechnics, Technical University of Budapest, Report*, (1).

Lei, X. Q., Yang, Z. J., He, S. M., Liu, E. L., Wong, H., & Li, X. P. (2017). Numerical investigation of rainfall-induced fines migration and its influences on slope stability. *Acta Geotechnica, 12*, 1431–1446.

Li, H., Cao, H. K., Li, X., & Qi, Z. P. (2024). Numerical study on urban hidden geological hazard detection based on the semi-airborne transient electromagnetic method. *Exploration Geophysics, 55*(4), 382–391.

Li, H., Xie, J. J., Fan, K. R., Li, W. H., & Li, X. (2025). Development of tunnel detection technology using the transient electromagnetic method in China. *Journal of Applied Geophysics, 233*, 105623.

Li, S. C., Xu, Z. H., Huang, X., Lin, P., Zhao, X. C., Zhang, Q. S., Yang, L., Sun, H. F., & Pan, D. D. (2018). Classification, geological identification, hazard mode and typical case studies of hazard-causing structures for water and mud inrush in tunnels. *Chinese Journal of Rock Mechanics and Engineering, 37*(5), 1041–1069 (in Chinese).

Liang, Y., Yeh, T. C. J., Ma, C., Zhang, Q., Yang, D. H., & Hao, Y. H. (2020). Experimental investigation of internal erosion behaviours in inclined seepage flow. *Hydrological Processes, 34*(26), 5315–5326.

Liu, Y. J., Yin, Z. Y., Wang, L. Z., & Hong, Y. (2021). A coupled CFD DEM investigation of internal erosion considering suspension flow. *Canadian Geotechnical Journal, 58*(9), 1411–1425.

Ma, Q. R., Wautier, A., & Zhou, W. (2021). Microscopic mechanism of particle detachment in granular materials subjected to suffusion in anisotropic stress states. *Acta Geotechnica, 16*(8), 2575–2591.

Marot, D., Tran, D. M., Bendahmane, F., & Le, V. T. (2020). Multidirectional flow apparatus for assessing soil internal erosion susceptibility. *Geotechnical Testing Journal, 43*(6), 1481–1498.

Mehdizadeh, A., Disfani, M. M., & Shire, T. (2021). Post-erosion mechanical response of internally unstable soil of varying size and flow regime. *Canadian Geotechnical Journal, 58*(4), 531–539.

Moukalled, F., Mangani, L., & Darwish, M. (2016). *The finite volume method in computational fluid dynamics: An advanced introduction with OpenFOAM® and Matlab®*. Springer.

Mu, L. L., Zhang, P. Y., Shi, Z. H., & Huang, M. S. (2023). Coupled CFD–DEM investigation of erosion accompanied by clogging mechanism under different hydraulic gradients. *Computers and Geotechnics, 153*, 105058.

Nguyen, C. D., Benahmed, N., Andò, E., Sibille, L., & Philippe, P. (2019). Experimental investigation of microstructural changes in soils eroded by suffusion using X-ray tomography. *Acta Geotechnica, 14*, 749–765.

Niu, X. D., Zhe, Y. L., Sun, H. F., Hou, K. P., & Jiang, J. (2023). Study on the effect of ore-drawing shear factor on underground debris flow in the Block Caving method. *Water, 15*(20), 3563.

Niu, X. D., Hou, K. P., Bao, G. T., & Zhe, Y. L. (2024). Study on formation mechanism of mud-inclusion-type underground debris flows using natural caving method. *Scientific Reports, 14*, 4324.

Norouzi, H. R., Zarghami, R., Sotudeh-Gharebagh, R., & Mostoufi, N. (2016). *Coupled CFD-DEM modeling: Formulation, implementation and application to multiphase flows*. John Wiley & Sons.

Oueidat, M., Benamar, A., & Bennabi, A. (2021). Effect of fine particles and soil heterogeneity on the initiation of suffusion. *Geotechnical and Geological Engineering, 39*(3), 2359–2371.

Peng, Z. B., Doroodchi, E., Luo, C. M., & Moghtaderi, B. (2014). Influence of void fraction calculation on fidelity of CFD-DEM simulation of gas-solid bubbling fluidized beds. *AIChE Journal, 60*(6), 2000–2018.

Pierce, M. E. (2010). *A model for gravity flow of fragmented rock in block caving mines*. [Doctoral dissertation, The University of Queensland, Australia].

Qian, Q. H. (2017). Main developments and directions of geological prediction and informatized technology of tunnel construction. *Tunnel Construction, 37*(3), 251–263 (in Chinese).

Ren, H. L., Zhuang, X. Y., Trung, N. T., & Rabczuk, T. (2021). Nonlocal operator method for the Cahn-Hilliard phase field model. *Communications in Nonlinear Science and Numerical Simulation, 96*, 105687.

Ren, H. L., Zhuang, X. Y., Zhu, H. H., & Rabczuk, T. (2024). Variational damage model: A novel consistent approach to fracture. *Computers & Structures, 305*, 107518.

Ren, H. L., Rabczuk, T., & Zhuang, X. Y. (2025). Variational damage model: A new paradigm for fractures. *Frontiers of Structural and Civil Engineering, 19*(1), 1–21.

Sterpi, D. (2003). Effects of the erosion and transport of fine particles due to seepage flow. *International Journal of Geomechanics, 3*(1), 111–122.

Sun, J. Q., Li, X. A., Li, J., Zhang, J., & Zhang, Y. T. (2023). Numerical investigation of characteristics and mechanism of tunnel erosion of loess with coupled CFD and DEM method. *Catena, 222*, 106729.

Tang, Y., Chan, D. H., & Zhu, D. Z. (2017). A coupled discrete element model for the simulation of soil and water flow through an orifice. *International Journal for Numerical and Analytical Methods in Geomechanics, 41*(14), 1477–1493.

Tofany, N., Low, Y. M., Lee, C. H., & Chiew, Y. M. (2019). Two-phase flow simulation of scour beneath a vibrating pipeline during the tunnel erosion stage. *Physics of Fluids, 31*(11), 113302.

Wan, C. F., & Fell, R. (2008). Assessing the potential of internal instability and suffusion in embankment dams and their foundations. *Journal of Geotechnical and Geoenvironmental Engineering, 134*(3), 401–407.

Xiong, H., Yin, Z. Y., Zhao, J. D., & Yang, Y. (2021). Investigating the effect of flow direction on suffusion and its impacts on gap-graded granular soils. *Acta Geotechnica, 16*, 399–419.

Xue, G. Q., Li, H., He, Y. M., Xue, J. J., & Wu, X. (2020). Development of the inversion method for transient electromagnetic data. *IEEE Access, 8*, 146172–146181.

Yan, Y., Tang, H., Hu, K. H., Turowski, J. M., & Wei, F. Q. (2023). Deriving debris-flow dynamics from real-time impact-force measurements. *Journal of Geophysical Research: Earth Surface, 128*(3), e2022JF006715.

Yan, Y., Tang, H., Zhou, K. L., Turowski, J. M., Cui, Y. F., & Xiang, B. (2025). Statistical characteristics of basal forces generated by experimental debris flows. *Journal of Geophysical Research: Solid Earth, 130*(3), e2024JB030027.

Yang, J., Yin, Z. Y., Laouafa, F., & Hicher, P. Y. (2020). Hydromechanical modeling of granular soils considering internal erosion. *Canadian Geotechnical Journal, 57*(2), 157–172.

Yang, J. C., Low, Y. M., Lee, C. H., & Chiew, Y. M. (2018). Numerical simulation of scour around a submarine pipeline using computational fluid dynamics and discrete element method. *Applied Mathematical Modelling, 55*, 400–416.

Yin, Y. Z., Cui, Y. F., Tang, Y., Liu, D. Z., Lei, M. Y., & Chan, D. (2021). Solid–fluid sequentially coupled simulation of internal erosion of soils due to seepage. *Granular Matter, 23*(2), 20.

Zhang, J., Feng, X. L., Wu, A. X., Cheng, H. Y., Li, Z. R., Wang, S. Y., Sun, W., & Chen, C. (2025a). Critical early warning of underground debris flows in mines based on rainfall–collapse characteristics. *Natural Hazards, 121*, 423–445.

Zhang, K., Shen, S. L., & Zhou, A. N. (2020). Dynamic brittle fracture with eigenerosion enhanced material point method. *International Journal for Numerical Methods in Engineering, 121*(17), 3768–3794.

Zhang, K., Shen, S. L., Zhou, A. N., & Balzani, D. (2021). Truncated hierarchical B-spline material point method for large deformation geotechnical problems. *Computers and Geotechnics, 134*, 104097.

Zhang, K., Shen, S. L., Wu, H., & Zhou, A. N. (2025b). Nitsche-based material point method for large deformation frictional contact problems. *Computational Particle Mechanics, 12*, 947–970.

Zhang, P. Y., Mu, L. L., & Huang, M. S. (2023). A coupled CFD DEM investigation into hydro-mechanical behaviour of gap-graded soil experiencing seepage erosion considering cyclic hydraulic loading. *Journal of Hydrology, 624*, 129908.

Zhang, Y., He, K., Hu, X. W., Liu, W. L., Zhang, S. L., Wu, J. L., & Xi, C. J. (2024). Mechanism of surface subsidence and sinkhole formation

in mining areas: Insights from MPM. *Bulletin of Engineering Geology and the Environment, 83*(8), 330.
Zhao, T., Houlsby, G. T., & Utili, S. (2014). Investigation of granular batch sedimentation via DEM–CFD coupling. *Granular Matter, 16*, 921–932.
Zou, Y. H., Chen, C., & Zhang, L. M. (2020). Simulating progression of internal erosion in gap-graded sandy gravels using coupled CFD DEM. *International Journal of Geomechanics, 20*(1), 04019135.